Light scattering in spin orbit coupling dominated systems

Von der Fakultät für Elektrotechnik, Informationstechnik, Physik
der Technischen Universität Carolo-Wilhelmina
zu Braunschweig
zur Erlangung des Grades eines
Doktors der Naturwissenschaften
(Dr.rer.nat.)
genehmigte
D i s s e r t a t i o n

von **Mehmet Fatih Çetin**
aus Eleskirt, Türkei

1. Referentin oder Referent: Prof. Dr. Peter Lemmens
2. Referentin oder Referent: Prof. Dr. Meinhard Schilling
3. Referentin oder Referent: Prof. Dr. Patrik Recher
eingereicht am: 24.08.2012
mündliche Prüfung (Disputation) am: 18.10.2012

2013

Vorveröffentlichungen der Dissertation

Teilergebnisse aus dieser Arbeit wurden mit Genehmigung der Fakultät für Elektrotechnik, Informationstechnik, Physik, vertreten durch die Mentorin oder den Mentor/die Betreuerin oder den Betreuer der Arbeit, in folgenden Beiträgen vorab veröffentlicht:

Publikationen

- Cetin, M. F., Lemmens, P., Gnezdilov, V., Wulferding, D., Menzel, D., Takayama, T., Ohashi, K., and Takagi, H., Crossover from coherent to incoherent scattering in spin-orbit dominated Sr_2IrO_4, Phys. Rev. B, **85**, 195148(2012)

  Tagungsbeiträge

  Präsentation

  - *Spin orbit coupling induced phonon anomalies and relevant electronic energy scales in* Sr_2IrO_4, DPG spring meeting, Dresden (2011)
  - *Comparative Raman study in spin orbit dominated iridates* Sr_2IrO_4, $Sr_3Ir_2O_7$, *and* $Na_4Ir_3O_8$, DPG spring meeting, Berlin (2012)

Abstract

Strong spin-orbit coupling (SOC) in solids has recently been identified as leading to novel electronic states with unconventional phases. Examples are topological insulators and unconventional magnets. Sr_2IrO_4, $Sr_3Ir_2O_7$, $BaIrO_3$, and $Na_4Ir_3O_8$ are candidates and model systems for such phases. Recent Resonant X-Ray and IR absorption studies on Sr_2IrO_4 show anomalies that are related to the proximity of charge and spin modes. This proximity is further investigated in the following thesis based on Raman scattering with different incident Laser energies (Resonant Raman scattering). Pronounced resonances show up in intensity and linewidths of phonon and magnetic scattering.

$Sr_3Ir_2O_7$ is another interesting case of spin orbit physics. Despite the similar crystal structure to Sr_2IrO_4, the electronic structure and magnetic structure of $Sr_3Ir_2O_7$ differs significantly from Sr_2IrO_4 which is evident in our magnetic Raman scattering data.

$BaIrO_3$ is a quasi-1D system which exhibits peculiar transitions. A charge density wave (CDW) formation accompanied by structural distortions is evident in our Raman scattering data in terms of electronic scattering and phonon anomalies. Another novel case of spin-orbit physics is given in $Na_4Ir_3O_8$ which is reported to be a spin liquid. First Raman data of this special compound are discussed.

Überblick

Neuartige elektronische Zustände in Festkörpern mit unkonventionellen Phasen basieren häufig auf starker Spin-Bahn-Kopplung (SOC). Beispiele dafür sind topologische Isolatoren und unkonventionelle Magnete. Die Verbindungen Sr_2IrO_4, $Sr_3Ir_2O_7$, $BaIrO_3$ und $Na_4Ir_3O_8$ dienen als Modellsysteme für solche Phasen. Aktuelle resonante Röntgen- (RIXS) und IR-Absorptionsstudien an Sr_2IrO_4 weisen Anomalien auf, die aus dem Zusammenspiel aus Ladung und Spin resultieren. Gegenstand der vorliegenden Arbeit ist die Untersuchung dieser Anomalien mittels Raman-Streuung mit unterschiedlichen Laser Energien (resonante Raman - Streuung). Ausgeprägte Resonanzen zeichnen sich in den Intensitäten und Linienbreiten von Phononen und magnetischer Anregung.

$Sr_3Ir_2O_7$ ist ein weiterer interessanter Fall von Spin-Bahn-Physik. Trotz der Sr_2IrO_4-ähnlichen Kristallstruktur weisen die Raman-Daten deutliche Unterschiede in den elektronischen und magnetischen Strukturen auf.

Das quasi-eindimensionale System $BaIrO_3$ zeichnet sich durch die Bildung einer Ladungsdichtewelle (CDW) durch strukturelle Verzerrungen aus, was zu Streu- und Phonon Anomalien in unseren Raman-Spektren führt.

Schließlich werden erste Raman-Spektren der Verbindung $Na_4Ir_3O_8$ gezeigt und diskutiert, die einen Spin-Flüssigkeitsgrundzustand ausbildet.

To my beloved mother, rest in peace...

Acknowledgements

This dissertation would not have been possible without the guidance and the help of several individuals who in one way or another contributed and extended their valuable assistance in the preparation and completion of this study.

Above all, I would like to express my deepest gratitude to my advisor, Prof. Peter Lemmens, for his excellent guidance, caring, patience, and providing me with an excellent atmosphere for doing research on such an exciting topic.

I would like to thank all my current and former colleagues: Dirk Wulferding, Hongdan Yan, Katharina Schnettler, Dr. Pushpendra Kumar, Dr. Viorel Felea, Johannes Dühn, Anshuma Pathak, Manuela Bosse, Ingrid Ringler, and Malte Schrader for providing me a great working environment. I specially thank Dirk Wulferding for his instructions and help with Raman setups and his valuable friendship. I also would like to thank to our guests Dr. Vladimir Gnezdilov, Prof. Yurii Pashkevich, Prof. Kwang-Yong Choi for fruitful discussions. I thank Dr. Dirk Menzel for XRD measurements and Prof. Jochen Littest, Prof. Stefen Süllow for constructive comments. I am grateful to Dr. Dezhen Li for her assistance. I acknowledge Dr. Ali Awada for his help with LaTeX word processor. I am also grateful to our technical staff Thilo Lampe,

Lutz Nagatz, Arno Ellermann for their help.

I would like to acknowledge Prof. Hide Takagi and his colleagues for providing us the single crystal samples of Sr_2IrO_4 and $BaIrO_3$ which made this research possible. I also would like to thank Chengtian Lin and his colleagues for the powder samples of $Sr_3Ir_2O_7$ and $Na_4Ir_3O_8$.

I am grateful to G. Jackeli and G. Khaliullin for the important discussions.

I am glad to acknowledge my valuable friends Burak Kutlu, Onur Kir and Alper Büyükkoz for their support, friendship and encouragement throughout this work.

This work was supported by NTH School "Contacts in Nanosystems", B-IGSM of the TU-Braunschweig and DFG.

Finally, I would like to thank to my parents and my family. They have given me their unequivocal support throughout, as always, for which my mere expression of thanks likewise does not suffice.

Contents

List of Figures

LIST OF FIGURES

List of Tables

LIST OF TABLES

Chapter 1

Introduction

In the past 15 years there has been a revolution in our understanding of generating, manipulating and detecting spin-polarized electrical currents which makes possible entirely new classes of spin-based sensor, memory and logic devices. Materials with large SOC could make the spintronic devices operating without an external magnetic field [1]. Large SOC induces an internal magnetic field which results e.g. in magnetic anisotropy. Magnetic anisotropy is crucial in terms of controlling the spin and creating exotic spin structures.

Iridium oxides are presently intensively studied to understand the interplay of strong SOC with correlation effects, not known from 3d transition metal oxides. This interplay is based on a different hierarchy of energy scales as well as on symmetry aspects of SOC. The latter may lead to, e.g. topological phases/excitations or enhanced spin-phonon coupling [2].

The unusual physics of Sr_2IrO_4 has two previously known fingerprints: small canted moments for $T<T_N$ that are related to the Mott insulating state as well as pronounced electronic resonances. Only recently it has been found that these

resonances consist of a group of dispersing/coherent spin as well as coherent and incoherent electronic modes that nearly overlap. The electronic modes consist of spin-orbit excitons and an electron hole continuum, respectively, and are based on an isospin $J_{eff} = 1/2$ manifold of states [3].

$Sr_3Ir_2O_7$ is a bilayer variant of the single layer Sr_2IrO_4. However, it has a much smaller charge gap and very different magnetic properties. In contrast to Sr_2IrO_4 with in-plane canted moments, $Sr_3Ir_2O_7$ has an easy c-axis collinear antiferromagnetic structure. It has been shown that the observed two-magnon excitations as a function of number of IrO_2 layers are due to the strong competition between intra- and inter-layer bond directional interactions of the spin-orbit entangled $J_{eff} = 1/2$ moments [4].

$BaIrO_3$ is a particularly interesting example of spin-orbit physics. It shows weak ferromagnetism with an unexpectedly high Curie temperature, charge-density-wave (CDW) formation, and a temperature-driven transition from weak-metal state to an insulating ground state [5]. The origin of the CDW anomaly has not been understood yet and we believe that Raman scattering can provide crucial information regarding the electronic dynamics of this quasi-1D system.

$Na_4Ir_3O_8$ was found to be a three dimensional network of corner sharing Ir^{4+} (t_{2g}^5) triangles which is called Hyperkagome lattice [6]. This yields an antiferromagnetically coupled $S = 1/2$ spin system formed on a geometrically frustrated hyperkagome lattice which is supposed to show no magnetic order at lowest temperature. However, in real materials, spin degeneracy can be lifted by coupling to other degrees of freedom such as orbital, lattice and charge. Raman scattering is a well established method to study such an interplay [7].

For a deeper understanding of theses systems it is of pivotal importance to

probe both lattice and electronic degrees of freedom simultaneously using suitable spectroscopic techniques. Questions to be addressed concern the typical energies and character of the excitations and whether temperature can be used to tailor the system from and anisotropic to an isotropic magnetism with possible novel excitations. Inelastic light scattering (Raman scattering), which is a non-destructive well established technique, probes lattice degrees of freedom as well as electronic correlations via a virtual electron-hole pair. The characteristic energy of this state can be tuned into resonance with the systems characteristic energies. To our knowledge such resonant optical experiments have not been performed on such systems[8].

Chapter 2

Theory

2.1 Spin Orbit Coupling in Solids

In this section, we follow in essence the lecture notes by Carsten Timm [9].

One of the most fascinating relativistic effects observed in solids (condensed matter systems) is that of the coupling between the orbital motion and the electron's intrinsic angular momentum, its spin. The physical origin of this coupling lies in the fact that in its frame of reference a spinning electron sees a time varying electric field generated by charges that are stationary. As a dynamic electric field induces a magnetic field, a magnetic coupling to the electron spin occurs. The magnitude of the effect depends on the local electric field, therefore, this phenomenon is associated with heavy atoms which can produce strong fields due to the large number of protons in their nuclei [10].

Semiclassical electrodynamics and non-relativistic quantum mechanics can be used to obtain a quantitative description of the spin-orbit interaction for an electron bound to an atom, up to first order in perturbation theory [11, 12].

We start with the energy of a magnetic moment:

$$\Delta H = -\mu \cdot B \tag{2.1}$$

where μ is the magnetic moment of the particle and the B is the magnetic field it experiences. Magnetic fields can be written in terms electron velocity v and the electric field it travels through E:

$$B = -\frac{v \times E}{c^2} \tag{2.2}$$

We know that E is radial for nucleus, so we can rewrite $E = |\frac{E}{r}|r$. Substituting this and the momentum of the electron $p = m_e v$ gives:

$$B = \frac{r \times p}{m_e c^2} \left| \frac{E}{r} \right|. \tag{2.3}$$

The electric field is the gradient of the electric potential $E = -\nabla V$. With central field approximation according to which the electrostatic potential is spherically symmetric, it is only function of radius:

$$|E| = \frac{\partial V}{\partial r} = \frac{1}{e}\frac{\partial U(r)}{\partial r}, \tag{2.4}$$

where $U = Ve$ is the potential energy of the electron in the central field, and e is the elementary charge. From classical mechanics, the angular momentum of a particle is $L = r \times p$. Putting it all together we get

$$B = \frac{1}{m_e c^2}\frac{1}{r}\frac{\partial U(r)}{\partial r} L. \tag{2.5}$$

The magnetic moment of the electron is:

$$\mu = -g_s \mu_B S/\hbar, \tag{2.6}$$

where S is the spin angular momentum vector, μ_B is the Bohr magneton and $g_s \approx 2$ is the electron spin g-factor. μ is a negative constant multiplied by the spin, so the magnetic moment is antiparallel to the spin angular momentum. The spin-orbit potential consists of two parts. The Larmor part is related to interaction of the magnetic moment of electron and the magnetic field of nucleus in the co-moving frame of electron. The second contribution comes from the Thomas precession. The Larmor interaction energy is:

$$\Delta H_L = -\mu \cdot B \tag{2.7}$$

Inserting Eq. 2.5 into Eq. 2.7 we get:

$$\Delta H_L = \frac{2\mu_B}{\hbar m_e c^2} \frac{1}{r} \frac{\partial U(r)}{\partial r} L \cdot S \tag{2.8}$$

Llewellyn Thomas relativistically recomputed the doublet separation in the fine structure of the atom [10]. The Thomas precession rate, Ω_T, is related to the angular frequency of the orbital motion, ω, of a spinning particle as shown below [13]

$$\Omega_T = \omega(1 - \gamma), \tag{2.9}$$

where the γ is the Lorentz factor of moving particle. The Hamiltonian producing

the spin precession Ω_T is given by

$$\Delta H_T = \Omega_T \cdot S. \tag{2.10}$$

To first order $(v/c)^2$, we get:

$$\Delta H_T = -\frac{\mu_B}{\hbar m_e c^2}\frac{1}{r}\frac{\partial U(r)}{\partial r} L \cdot S. \tag{2.11}$$

Finally the total spin-orbit potential in an external electrostatic potential can be written in the form of

$$\Delta H \equiv \Delta H_L + \Delta H_T = \frac{\mu_B}{\hbar m_e c^2}\frac{1}{r}\frac{\partial U(r)}{\partial r}(L \cdot S). \tag{2.12}$$

Starting with Dirac equation and calculating small corrections from quantum electrodynamics would result in a more precise equation, however, this Hamiltonian gives results which describe the experimental observations well.

2.2 Fundamentals of Inelastic Light Scattering

In this section, we follow in essence the review articles by Lemmens et al. [14, 15].

When monochromatic light with frequency ω_I, polarization $\vec{e}_I$ and the external electric field $\vec{E}_I(\omega, \vec{r})$ encounters matter, a polarization $\vec{P}(\omega, \vec{r})$ in the medium is induced. Light of spectral density $\rho(\vec{q}, \omega)$ is scattered by the medium with frequency $\vec{\omega}_S$ and polarization $\vec{e}_S$ as it is shown in Fig.2.1a. The intensity I of this dipole-radiation is proportional to the fourth power of frequency. Such inelastic scattering effect was discovered by V.C. Raman and by G.S. Landsberg

and L.I. Mandels'shtam independently in 1928 and called Raman Scattering (RS). If the frequency the so called Raman shift $\omega = \omega_I - \omega_S$ is negligible ($\omega_S \approx \omega_I$) the process is elastic and called Rayleigh scattering. On the other hand, for $\omega_S < \omega_I$ or $\omega_S > \omega_I$, the scattering is named Stokes or anti-Stokes, respectively.

A polarization $\vec{P}$ induced by scattering is related to the electronic susceptibility tensor $\chi(\omega)$, a property specific to the material, by the response relation $\vec{P}(\omega, \vec{r}) = \epsilon_0 \chi(\omega) \vec{E}(\omega, \vec{r})$. χ is constant in space and time in uniform medium. The Huygens-Fresnel principle suggests that secondary waves from different points inside the incident beam cancel each other out, see Fig.2.1b. Spatial and temporal fluctuations of χ in the medium lead to scattering processes. The spectral density of the scattered light is defined by a correlation function of the fluctuations:

$$\rho(q, \omega) \sim \int < \delta\chi^*(q, t)\delta\chi(q, 0) > e^{i\omega t} dt, \tag{2.13}$$

where $\vec{q} = \vec{k_I} - \vec{k_S}$ and $\omega = \omega_I - \omega_S$ are the change of the wave vector and wave number according to their conservation in the scattering process. Density fluctuations or internal degrees of freedom such as phonons generate the fluctuation spectrum $\chi(\omega)$ in solids. Density fluctuations result in a weak scattering continuum that quickly decreases in intensity as function of Raman shift while the phonons lead to peaks in $\rho(\omega)$ at the frequencies corresponding to the energy of excitations. These energies range typically from 50 to 1000 cm^{-1} for phonons in solids and goes up to 3500 cm^{-1} for molecular vibrations. The conventional unit for Raman shift, *wave number*, [cm^{-1}], is the difference of inverse of the corresponding wavelength λ in [cm] and can be written in other units as follows; $1\,[\mathrm{cm}^{-1}] \approx 1.44\,[\mathrm{K}] \approx 1/8\,[\mathrm{meV}] \approx 33\,[\mathrm{GHz}]$.

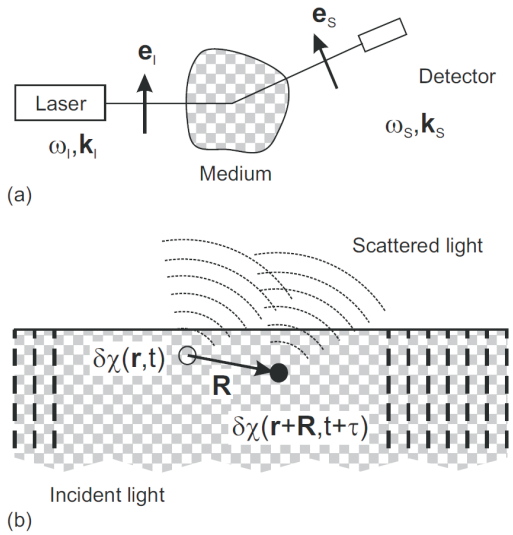

Figure 2.1: a) Schematic description of light scattering geometry and b) interference of secondary waves from different points inside the incident beam [15].

2.2.1 Quantum Mechanical Approach

Incident photons of energy $\hbar\omega_I$ and momentum $\hbar\vec{k}_I$ yield photons of energy $\hbar\omega_s$ and momentum $\hbar\vec{k}_s$ in inelastic scattering processes. Meanwhile, the crystal in an initial state, i, with energy E_i is excited to a final state, f, with energy E_f. Fermi's rule of second order perturbation theory formulates the probability of scattering, P_{if} as below

$$P_{if} = \frac{2\pi}{\hbar}\rho_{dos}(\omega_S)|H(\vec{k_I}, i : \vec{k_S}, f)|^2\delta(\hbar\omega_I + E_i - \hbar\omega_S - E_f), \tag{2.14}$$

where $\rho_{dos}(\omega_S)$ is the density of states of photon which is given by $\rho(\omega_S)d\omega_S d\Omega = (1/2\pi c)^3\omega_S^2 d\omega_S d\Omega/\hbar$ and $d\Omega$ is a solid angle. Considering that the sizes of atoms are much smaller than the wavelength of incident/scattered light, the effective

Hamiltonian can written in terms of polarization as

$$H(\vec{k_I}, i : \vec{k_S}, f) = \sum_{r,\alpha,\beta} E_{\mathrm{I}}^{\alpha}\, \chi^{\alpha\beta}(r)\, E_S^{\beta}\ , \tag{2.15}$$

where α and β denotes Cartesian coordinates. The photon creation [annihilation] operator, $b^{\dagger}(k)[b(k)]$ describes the electric field;

$$\vec{E_I} = i\sqrt{2\pi\hbar\omega_I} E_I \vec{e}_I [b(\vec{k}_I) - b^{\dagger}(-\vec{k_I})], \tag{2.16}$$

where $\vec{e_I}$ is the polarization vector of photon. The total Raman scattering intensity is obtained using these results:

$$I_R \sim \omega_I \omega_S^3 \int \ll \chi(\vec{k_I}\vec{k_S}; t)\chi^{\dagger}(\vec{k_I}\vec{k_S}; 0) \gg e^{i\omega t} dt. \tag{2.17}$$

It consists of the thermodynamic average (denoted with bracket, $\ll \cdots \gg$) of a pair of correlation function of the fluctuating polarization. Dipol matrix elements $< f|\vec{M}_\beta|i >$ with moments $\vec{M}_\alpha = er_\alpha$ between the initial and final states provide an explicit form of the susceptibility with $\omega_{fi} = [E_f - E_i]/\hbar$:

$$\chi_{\alpha\beta}(\omega) = 2\sum_{i,f} < i|\vec{M}_\alpha|f >< f|\vec{M}_\beta|i > \times [\frac{1}{\omega_{fi} - \omega} + \frac{1}{\omega_{fi} + \omega}] \frac{d^3k}{(2\pi)^3}. \tag{2.18}$$

Factor 2 is due to the spin.

Phonon Scattering

Phonon modes usually dominate RS intensity of solids. Lets consider an acoustic phonon $\nu(= 1, ..., 3N_c)$ with N_c the number of ions per unit cell. In adiabatic approximation a phonon consists of atomic displacements with the eigenvector

Q_ν. These vectors can be treated as a very slow ionic displacement yielding a *static* potential within the unit cell $\delta U_\nu(r)$. The energy of the initial state will be shifted by $\delta E_{i,\nu} =< i|\delta U_\nu(r)|i >$ due to this slow varying potential. Moreover the band wave function is changed as $\delta|i >= \sum_{f\neq i} \frac{<i|\delta U_\nu(r)|i>}{E_f - E_i}|f >$. Therefore the susceptibility tensor in Eq. 2.18 changes to:

$$\delta\chi_\nu^{\alpha\beta} = \sum_{a=1}^{N_c} Q_{a,\nu} \frac{\partial\chi^{\alpha\beta}(\omega)}{\partial Q_a} \tag{2.19}$$

which results in a scattering intensity at the phonon frequency Ω_ν:

$$\rho(\omega) = \frac{1}{\pi} I_R \frac{\gamma_\nu}{(\omega - \Omega_\nu)^2 + \gamma_\nu^2} \tag{2.20}$$

γ_ν and I_R denote phonon linewidth and scattering intensity, respectively. Putting Eq. 2.18 into Eq. 2.19 shows that the integrated intensity of phonons consists of two contributions: the band energy on the ion configuration, $\partial\omega_{fi}/\partial Q_a$, gives the first contribution and the polarization of band wave functions and the change in the interionic distance $\partial < f|\vec{M}_\alpha|i > /\partial Q_a$. Because of the large difference between the photon energy ($\hbar\omega_I \approx 1.5 - 2.5\,\mathrm{eV}$) and the phonon energy ($< 100\,\mathrm{meV}$), phonon RS does not arise from direct light-phonon interaction, but occurs instead from third order time dependent perturbation theory.

The RS process consists of three virtual electronic transitions that could be explained in three steps: (i) A virtual electron-hole pair state is excited by the incident photon due to the electron-radiation coupling. (ii) Transition of the electron (Stokes process) or hole (anti-Stokes) to a different state is induced by electron-phonon coupling. (iii) Recombination of electron-hole pair emitting the scattered photon causes transition to the electronic ground state.

The Hamiltonian of a phonon excitation can be written as:

$$H_R = -\frac{e}{mc}\vec{p}\cdot\vec{A} + \sum_{ijk} g_{ij}(k)(b^\dagger + b)c_{ik}^\dagger c_{jk}, \tag{2.21}$$

where $g_{ij}(k)$ denotes the electron-phonon coupling between the band i and j. $b^\dagger(b)$ and $c_{ik}^\dagger(c_{jk})$ are the phonon and electron creation(annihilation) operators, respectively. The first term of Eq. 2.21 represents electron-radiation interaction including step(i) and step(iii) which describes a scattering process via an intermediate state causing an interband transition. The second term in Eq. 2.21 is a linear contribution in terms of the electron-phonon interaction.

Semiconductors and insulators have higher polarizability and penetration depth in comparison to metals, therefore the scattering cross section for these materials is substantial. Thus, higher order RS can give important information about the electronic structure of semiconductors and insulators due to their significantly large scattering cross section. The microscopic origin of two-phonon processes can be understood by writing electron-phonon interaction Hamiltonian up to the quadratic term:

$$H_{e-p} = \sum_q g_1(q)(b_{-q}^\dagger + b_q)c_{k+q}^\dagger c_k + \sum_q g_2(q)(b_{q_1}^\dagger b_{q_2}^\dagger + b_{q_1}^\dagger b_{q_2} + b_{q_1} b_{q_2})c_{k+q}^\dagger c_k, \tag{2.22}$$

where g_2 is the anharmonic interaction constant. Lattice anharmonicity yields a simultaneous emission of two phonons which is shown with the second term of the Hamiltonian (Eq. 2.22). On the other hand, two phonons are created separately as result of the first order electron-lattice interactions and this is introduced by second term of Eq. 2.22. This process includes an additional virtual electron state

along with the creation of two phonons which can be in resonance if the energy of the excitation light coincides with this virtual electronic state. The maximum in a plot of two phonon scattering intensity as a function of energy of the excitation light, corresponds to the interband energy. In a two phonon creation process, energy and momentum is conserved:

$$\omega_{\sigma q} + \omega_{\sigma' q'} = \omega_I - \omega_S \tag{2.23}$$

$$\vec{q} + \vec{q'} = \vec{k_I} - \vec{k_S}, \tag{2.24}$$

where σ and σ' denote the phonon branches. Therefore, it can be seen that total momentum of a pair of emitted phonons $\vec{q} + \vec{q'} = 0$ should vanish due to the restricted phonon scattering to a regime near the Γ-point of the Brillouin zone. As a result, both wave vectors $\vec{q}$ and $-\vec{q}$ have the same frequencies. Therefore the energy conservation is written as $\omega_{\sigma q} + \omega_{\sigma' q'} = \omega_I - \omega_S$ which shows that a combination of density of states of phonon pairs provides the second-order light-scattering phonon spectrum,

$$\rho_2(\omega) = \sum_{\sigma,\sigma'} \sum_{q} \delta(\omega - \omega_{\sigma q} - \omega_{\sigma' q}). \tag{2.25}$$

This shows that higher-order scattering gives indirect information about the whole Brillouin zone in contrast to one-phonon scattering.

The number of Raman active phonons and their selection rules (measurement geometry) can be determined by using group theory in the following steps; determination of site symmetry of each atom in the unit cell of the compound, finding the corresponding irreducible representations (phonon) and subtracting the RS

active ones from the silent and infrared active modes. Necessary information for these steps can be obtained from crystallographic data bases [16]. Furthermore, calculation or assignment of phonon frequencies can be done using theoretical models, i.e shell lattice or in situ calculations, or a comparison to a known compound with the same crystal structure.

The phonon modes are classified according to their representations' dimensionality such as 1-dim. (A_{1g} or B_{1g}), 2-dim. (E_{2g}) or 3-dim. (T_{1g} or F_{1g}). A and B denote a *positive/negative* value of polarizability χ with respect to the rotation about the principle axis. The index g stands for *gerade* and u stands for *ungerade* with respect to the inversion center. Moreover, the numbers 2 and 3 are used to indicate a symmetry with respect to other rotations or with respect to reflections. An example for irreducible representation of Raman-active modes is shown below;

$$\Gamma_{Raman} = A_{1g} + B_{1g} + B_{2g} + 2{\cdot}E_g \tag{2.26}$$

This shows that in total five Raman active modes are expected. Different modes are allowed in different scattering geometries according to their Raman tensors which are shown in Eq. 2.27;

$$A_{1g} : \begin{pmatrix} a & 0 & 0 \\ 0 & a & 0 \\ 0 & 0 & b \end{pmatrix}, B_{1g} : \begin{pmatrix} c & 0 & 0 \\ 0 & -c & 0 \\ 0 & 0 & 0 \end{pmatrix}, B_{2g} : \begin{pmatrix} 0 & d & 0 \\ d & 0 & 0 \\ 0 & 0 & 0 \end{pmatrix} \tag{2.27}$$

$$E_g : \begin{pmatrix} 0 & 0 & e \\ 0 & 0 & f \\ e & f & 0 \end{pmatrix}$$

The modes with A_{1g} symmetry are allowed in parallel polarization of incident and scattered light to a crystallographic axis. However, modes with B_{2g} symmetry can be observed only if the incident light ($\vec{e_I}$) is perpendicular to scattered light ($\vec{e_S}$).

Electronic Scattering

Scattering due to the fluctuations of effective charge density in electronic systems can also contribute to the Raman response. The effective charge density is expressed by the curvature of the bands, if the energy of exciting photons is smaller than a band gap energy. In this case, a contribution from fluctuations of the effective mass tensor dominates the electronic RS. Unlike real charges, the effective charge density is not conserved. However, in pure metals, screening suppresses the electronic RS. This can be formulated by taking the Lindhard expression in the limit of small wave vector. Very important information regarding lifetime or scattering rate of quasiparticles can be obtained by electronic RS in strongly correlated electron systems. Materials with a metal-insulator transition such as Kondo systems, mixed-valence materials, and underdoped high-temperature superconductors, demonstrate a strong spectral rearrangement of electronic RS. In systems with an anisotropic gap, electronic RS intensity shows a strong polarization dependence. Therefore polarization dependent RS is a powerful tool to probe the anisotropy in such systems.

Magnetic Scattering

The study of spin waves or magnons in ferromagnetic and antiferromagnetic compounds by light scattering is a well established method. Magnetic light scattering

can be used to determine coupling constants, anisotropies and magnon-magnon interactions. Magnons induce a spatially periodic modulation in susceptibility tensor. The modulation of $\chi^{\alpha\beta}(r)$ can be written as Taylor expansion of spin operators:

$$\begin{aligned}\chi^{\alpha\beta}(\mathbf{r}) = \quad & \chi_0^{\alpha\beta}(\mathbf{r}) + \sum_{\mu} \mathrm{K}_{\alpha\beta\mu}(\mathbf{r})\mathrm{S}_{\mathbf{r}}^{\mu} \quad + \sum_{\mu,\nu} \mathrm{G}_{\alpha\beta\mu\nu}(\mathbf{r})\mathrm{S}_{\mathbf{r}}^{\mu}\mathrm{S}_{\mathbf{r}}^{\nu} \\ & + \sum_{\delta}\sum_{\mu,\nu} \mathrm{M}_{\alpha\beta\mu\nu}(\mathbf{r},\delta)\mathrm{S}_{\mathbf{r}}^{\mu}\mathrm{S}_{\mathbf{r}+\delta}^{\nu} \quad + \text{higher order terms}\end{aligned} \tag{2.28}$$

The coefficient tensors K, G, and M correspond to the strength of the coupling between light and the magnetic system. The first term in this equation is due elastic scattering while the second and third term are linear and quadratic in spin operators, respectively. The linear term in S_r^{μ} is the combination of one magnon creation (S_r^+) and annihilation (S_r^-) processes. The quadratic term at a *single* ionic site $\mathbf{r}$ also leads to one-magnon scattering. This term can be reformulated in terms of a linear and transverse spin operator as $S_r^+ S_r^z$, $S_r^z S_r^+$, $S_r^- S_r^z$, and $S_r^z S_r^-$. Moreover, the quadratic spin term at different sites also has an effect on the one-magnon scattering due to the terms proportional to $S_r^+ S_{r+\delta}^z$, $S_r^z S_{r+\delta}^+$, $S_r^- S_{r+\delta}^z$, and $S_r^z S_{r+\delta}^-$.

This fundamental explanation of one-magnon scattering can be obtained from a microscopic mechanism of spin-orbit coupling. Let's consider a ground state with zero orbital momentum and spin S as depicted in Fig. 2.2 (a). This state will be split into (2S+1) components by the effective magnetic field. One can assume an excited orbital state with $L = 1$ and the same S as the ground state. This excited state also splits into three components corresponding to $J = S+1, S$, and

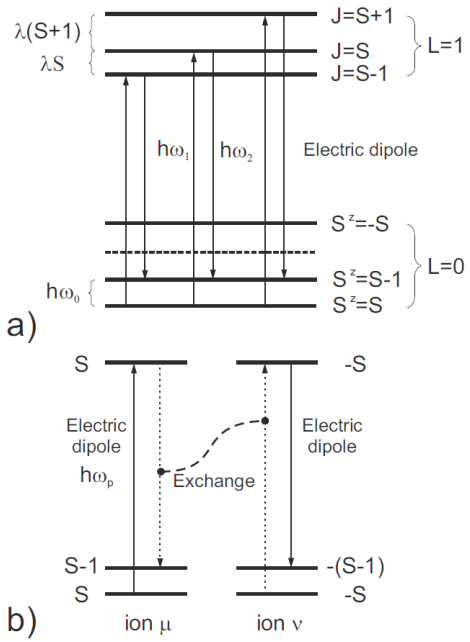

Figure 2.2: a) one-magnon scattering process and b) two-magnon exchange scattering [15].

$S-1$ by spin-orbit interaction $\lambda L{\cdot}S$, where λ is the spin-orbit coupling strength. Every excited state $|J, J^z>$ is a linear combination of the unperturbed $|L^z, J^z>$ states. Afterwards, the transition from $S^z = S$ ground state to $S^z = S-1$ occurs by a sequential electric dipole transition via the $L = 1$ virtual intermediate state. Hence, the coupling constant K can be derived from the spin-orbit coupling strength λ.

Two-magnon scattering is a result of a different process. It has a larger scattering cross section in comparison to one-magnon process even though it is a higher order scattering which is based on a double spin-flip. This spin-flip is caused by matrix elements of the Coulomb interaction conserving the total z component of spins. In Fig. 2.2 (b), the scattering mechanism is shown. Two ions μ and ν, have an electron each r_1 and r_2 with $S^z = \frac{1}{2}(\uparrow)$ in an orbital $|\mu>$

and $S^z = \frac{1}{2}(\downarrow)$ in an orbital $|\nu>$ at ground state. The simultaneous change of the spin components of ions μ and ν in the electric dipole interaction is second-order while the exchange interaction between two electrons via Coulomb interactions is first-order. Consequently, the effective spin exchange Hamiltonian can be written as:

$$H_{2-mag} \propto \sum_{ij} E_S^i E_I^j S_\mu^- S_\nu^+. \tag{2.29}$$

The same exchange mechanism including the Coulomb interaction is relevant to both Heisenberg and two-magnon Hamiltonians, therefore they both have the same form. Via two-magnon scattering not only exchange constants and magnon-magnon interactions but also even short range correlations of exchange coupling can be probed as the two-magnon process is effective for nearest neighbor spins of an antiferromagnetic system.

2.2.2 Experimental Set-up

A sketch of our RS setup is shown in Fig. 2.3. It is possible to optimize inelastic light scattering setups for high resolution and quasi-elastic light filtration or for small sample and surface characterization with a microscope. They consist of the following important elements:

Monochromatic light source: Frequency doubled Laser diodes or Nobel gas (helium/neon, argon, krypton) ion Lasers can be used as light source in inelastic light scattering experiments. Nobel gas ion lasers are crucial for resonance Raman experiments. We use a plasma filter in order to cut out the side contributions to output frequency different from the desired one (plasma lines). The polarization of the laser beam is tuned by using a $\lambda/4$ and $\lambda/2$ wave plates. The

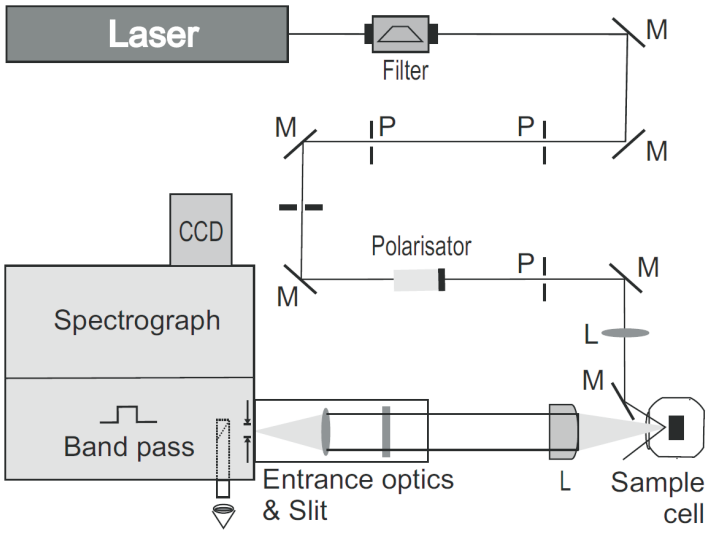

Figure 2.3: RS setup in quasi-backscattering geometry constructed with a spectrometer, mirrors (M), pinholes (P) and lenses (L) [15].

light power level on the sample is typically around 4-20 mW with a focus diameter of 50-100 μm. In the case of the Raman microscope a lower power level with a focus diameter of 1-5 μm is applied.

Scattering configuration: As the solid samples investigated in this thesis are opaque, a quasi-backscattering configuration is preferred. Samples are slightly canted with respect to the incident light beam to eliminate the quasi-elastic light. Measurement conditions of RS i.e. temperature and vacuum, are conveniently changed by using a cryostat. Only one set of window material (fused silica) is required as the Raman shift of the scattered light is small in comparison to the incident frequency, $\Delta\omega/\omega_I \approx 10^{-2}$. The back scattered light is collected with a lens (e.g. photographic lens) and focused on the entrance slit of a monochromator after filtration with respect to polarization. For the optical alignment, a camera with a view on the sample is mounted behind the open entrance slit. Confocal entrance optics (spacial filtering) is useful to improve the focus.

Monochromator and detection: Surface roughness and Rayleigh scattering can cause significant quasi-elastic light which needs to be filtered out. A subtractive double monochromator is used as a band pass to eliminate this light. A single monochromator stage with blazed, holographic gratings is used to disperse the transmitted light on the detector. A charge coupled device (CCD) serves as a detector in our RS setups. This array detector allows simultaneous detection of a broad frequency band. It has a single photon sensitivity with quantum efficiencies of up to 80 %. Accumulation times of 10 sec. to 5 min. are selected depending on the Raman signal strength. Averages of several measurements are taken to acquire a reasonable signal/noise ratio and to eliminate the spikes induced by cosmic muons in the detector.

Chapter 3

Light Scattering in SOC Materials

3.1 The 2D compound Sr_2IrO_4

In this section, we follow in essence our article by Cetin et al. [8].

In correlated electron systems novel quantum phases and properties result very often from an uncommon hierarchy of energy scales. Recent interesting cases concern spin-orbit coupling (SOC) comparable or even superior to Coulomb energies [17]. Spin-orbit coupling is relevant for several $4d$ and $5d$ systems, such as the iridates $Na_4Ir_3O_8$ and Na_2IrO_3 with a spin liquid [6] and a topological insulating [18] state, respectively, and Sr_2IrO_4 as a special Mott insulator [19]. In strongly correlated $3d$ electron systems SOC is usually comparably small leading to moderate changes of the magnetic excitations by anisotropy gaps in the long range ordered state. With only few exceptions magnetic modes are strictly decoupled from charge excitations. However, with strong SOC the spin excitation spectra

differ considerably from those of $3d$ systems. This is due to topological effects as well as the mixing with orbital and charge excitations. It is presently a matter of debate which consequences this overlap and interaction has for charge excitations close to the optical (Mott-Hubbard) gap [18].

Sr_2IrO_4 has a distorted tetragonal structure, known from some cuprates, with magnetic ions ($Ir^{4+}, 5d^5$) on a square plane connected by oxygen ions forming octahedra. The compound shows antiferromagnetic (AFM) order with canted, in-plane, ferromagnetic moments ($0.14\,\mu_B$ per Ir) and enhanced structural distortions given by in-plane rotations of the IrO_6 octahedra for $T<T_N = 240\,K$ [20]. The rotations and the moments are directly related via SOC [21]. For lower temperatures further anomalies are observed, e.g. an enhanced electric permittivity at around 100 K which is attributed to modulations of the Ir-O-Ir bond angle [22].

The Ir^{4+}low lying t_{2g} states form lower $J_{eff} = 3/2$ and higher energy $J_{eff} = 1/2$ isospin states with a splitting given by the large SOC coupling constant 0.4 eV [23]. With 5 electrons this situation corresponds to a single band with $J_{eff} = 1/2$ [19]. More conventional $5d$ compounds have a higher conductivity. This hints towards an unusual Mott state in Sr_2IrO_4 with narrow, spin-orbit induced $J_{eff} = 1/2$ states that are susceptible to electronic correlations [21]. Using the phase sensitivity of resonant inelastic X-Ray scattering (RIXS) the J_{eff} level scheme has been directly probed [24]. Interband transitions across the Mott gap and charge-transfer excitations from the low energy O $2p$ band to the Ir $5dt_{2g}$ bands (upper Hubbard band) and to the Ir e_g $3z^2 - r^2$ states show up with characteristic energies of 0.5, 2.5/3.2, and 6.0 eV [25]. The 2.5 and 3.2 eV mode correspond to the same dispersing charge transfer excitation. Nevertheless, these

modes are coherent and represent a small dispersion of the Mott gap in contrast to theory [17]. More recently a strongly dispersing, lower energy mode (0.4 - 0.8 eV) has been observed and related to spin-orbit excitons of the J_{eff} states [3].

The above mentioned energies are in good agreement with optical absorption studies [26, 27]. The optical absorption renormalizes gradually with increasing temperatures which is interpreted as a reduction and filling up of the Mott-Hubbard gap with temperature. Optical spectroscopy experiments also show phonon anomalies, e.g. a 3 % softening of a phonon mode at 660 cm^{-1} that modulates the Ir-O-Ir bond angle [26, 27]. A list of these phonons is given in 3.2 together with Raman active modes.

3.1.1 Crystal Structure

The crystal structure of Sr_2IrO_4 is $D_{4h}{}^{20}$ - $I4_1/acd$, Nr. 142 [20] and is derived from a distorted K_2NiF_4 (I4/mmm)-type tetragonal structure. This structure is illustrated in Fig. 3.1. It belongs to the tetragonal - ditetragonal dipyramidal class (4/m 2/m 2/m), with four 2-fold and one 4-fold axes including a center of inversion. Neutron and diffuse X-ray scattering patterns show positive deviations from the patterns calculated for $I4_1/acd$ space group. These observations are assigned to rotations of the IrO_6 octohedra. IrO_6 octahedra are rotated about the c-axis by around 12°. This tilting angle is temperature dependent. Moreover, the IrO_6 rotations in Sr_2IrO_4 are correlated along $c-$axis which yields superlattice reflections. It is noteworthy to mention that, similar to the CuO_6 octahedra in La_2CuO_4 which is also a canted antiferromagnet (AFM), IrO_6 octahedra are elongated in the c direction. This can be a Jahn-Teller distortion or an effect of

the anisotropic crystal structure [20].

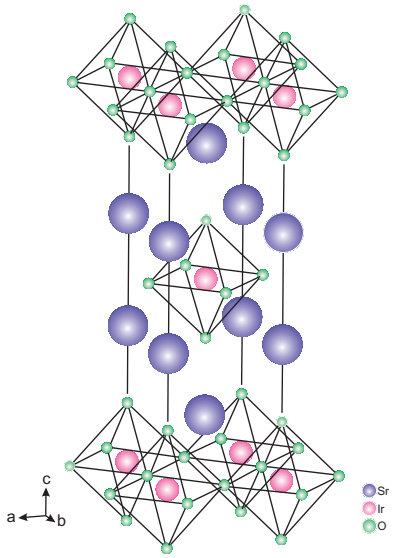

Figure 3.1: Crystal structure of Sr_2IrO_4 [20].

3.1.2 Electronic and Magnetic Properties

The electronic configuration of the Ir^{4+} ions is [Xe]d$f^{14}5d^5$. Compared to $3d$ electrons, $5d$ electrons are more delocalized which is expected to yield weakly correlated wide bands with largely reduced on-site Coulomb repulsion U. Therefore, considering its odd number of electrons per unit formula ($5d^5$), Sr_2IrO_4 is expected to be metallic in naive band picture [21]. However, Sr_2IrO_4 is surprisingly an insulator with weak ferromagnetism [20].

Many studies have been done to explain this peculiar electronic structure. These studies have shown that electronic states near E_F significantly depend on SO coupling in $5d$ systems [28]. Kim et al. suggest the following model which is also confirmed by ARPES, optical conductivity and x-ray absorption spectroscopy (XAS) experiments to explain the band structure of Sr_2IrO_4 [21].

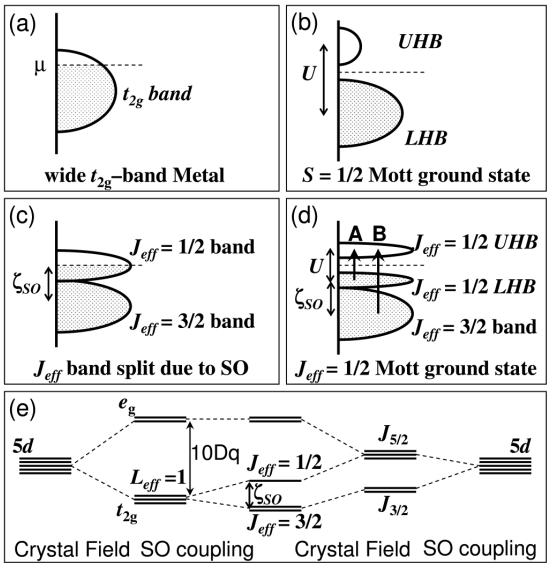

Figure 3.2: Schematic energy diagrams for $5d^5(t_{2g}^5)$ configuration (a) without SO and U, (b) with an extremely large U but no SO, (c) with SO but no U, and (d) with SO and U. Allowed optical transitions A and B are shown with arrows. (e) $5d$ level splittings induced by crystal field and SO coupling [21].

Under O_h symmetry, the crystal field energy 10Dq splits the $5d$ states into t_{2g} and e_g orbital states. Normally, $4d$ and $5d$ TMOs have a large enough crystal field, 10Dq, to result in a t_{2g}^5 low-spin state for Sr_2IrO_4. In this case the system would be a metal with a partially filled, wide t_{2g} band (Fig. 3.2(a)). Only an extremely large U ($\gg W$) could yield a spin $S = 1/2$ Mott insulator, Fig. 3.2(b); because a reasonable U can not lead to an insulating state as seen from the fact that Sr_2RhO_4 is a normal metal. In the presence of strong SO coupling, the t_{2g} band is split into *effective* total angular momentum $J_{eff} = 1/2$ doublet and $J_{eff} = 3/2$ quartet bands, Fig. 3.2(c). This t_{2g} level splitting could be also because of lattice distortions, however XAS shows that distortion effects in Sr_2IrO_4 are minimal. Consequently, the system is effectively reduced to a half-filled $J_{eff} = 1/2$ single band system with the filled $J_{eff} = 3/2$ band and

one remaining electron in the $J_{eff} = 1/2$ band, Fig. 3.2(c). The $J_{eff} = 1/2$ spin-orbit induced states have such a narrow band width that even a small U creates a Mott gap, Fig. 3.2(d). The narrow band width can be explained by a reduced hopping integral of the $J_{eff} = 1/2$ states due to isotropic orbital and mixed spin behaviors. J_{eff} bands that are induced by large ζ_{SO} are the reason for Sr_2IrO_4 ($\zeta_{SO}\sim 0.5\,eV$) being insulating while Sr_2RhO_4 ($\zeta_{SO}\sim 0.15\,eV$) is metallic [21]. More recently, interband transitions across the Mott gap together with the charge transfer excitations from the O2p to the $5d\ t_{2g}$ states are probed by optical conductivity [26, 27] and resonant inelastic x-ray scattering (RIXS) experiments, [24, 25] confirming the scenario suggested by Kim et al. [21].

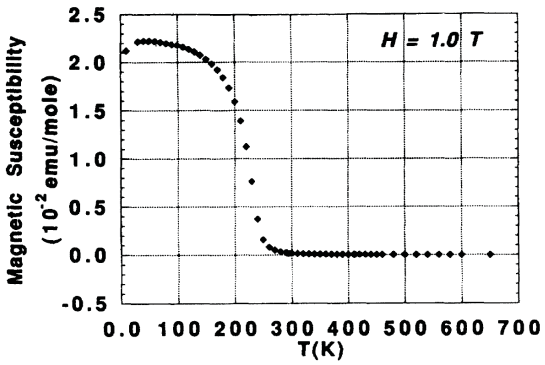

Figure 3.3: Temperature dependent magnetic susceptibility of Sr_2IrO_4 [20].

Magnetic properties of Sr_2IrO_4 are first investigated by Crawford et al. and Cao et al [29]. They report magnetic susceptibility as a function of temperature in which there is a distinct magnetic transition at approximately 250 K, see Fig. 3.3. They perform magnetic hysteresis measurements to clarify the nature of this magnetic transition. A substantial magnetic hysteresis is evident in their data suggesting a ferromagnetic component in the magnetic structure. They attribute the ferromagnetic behavior to canted antiferromagnetism. Dzyaloshinskii-Moriya

(DM) interaction which arises as a result of the structural distortion described in 3.1.1 is suggested as the origin of canted antiferromagnetism. The canted moment ($\sim 10^{-2}\mu_B$) and the rotational distortions of the IrO_6 octahedra ($\sim 12°$) in Sr_2IrO_4 is 1 order of magnitude larger than the moment ($\sim 10^{-3}\mu_B$) and the rotational distortions of the CuO_6 octahedra ($\sim 3°$) in La_2CuO_4. However, Jackeli et al. claim that rotational distortions alone are not enough to explain such an unusually large FM moment. Therefore they suggest quantum compass and Kitaev models in which Hamiltonians are extrapolated from Heisenberg in the strong spin orbit coupling limit [23].

Crawford et al. also claim that these canted moments are ferromagnetically aligned in successive layers in contrast to the situation in La_2CuO_4 where the canted moments are antiferromagnetically ordered in successive layers. However, later RIXS studies by Kim et al. [24] show that the moments are, in fact, aligned antiferromagnetically within the layers along c axis. They confirm that canting of the moments yields a nonzero net moment within a layer, which orders in the up-down-down-up antiferromagnetic pattern along the c axis, which is evidenced by the presence of (0 0 *odd*) RIXS peaks. In 2009 Chikara et al., report magnetic data in which a giant magnetoelectric effect(GME) and further magnetic anomalies are present [22]. They observe a downturn of magnetization at around 100 K which is substantially temperature and field dependent. μSR measurements by Franke et al. detect further magnetic anomalies. Sr_2IrO_4 shows no oscillatory signal in μSR spectra above the ordering temperature as it is expected for paramagnets. Between T_N and 20 K, μSR spectra could be fitted by using one oscillation and one exponentially relaxing component. However, below 20 K a second frequency is required to obtain a satisfactory fit to the data which is unknown and does not

correlate with any previously reported magnetic transition [30].

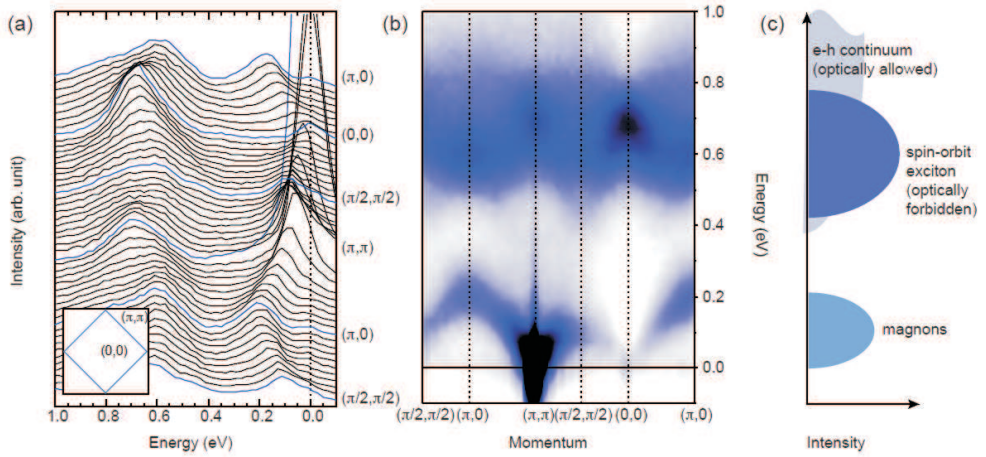

Figure 3.4: Energy loss spectra measured at $T = 15\,\mathrm{K}$ (a), image plot (b) and the schematic representation (c) of the data shown in (a) [3].

The magnetic exchange interaction J for this system is estimated to be around 80 meV by using variational Monte Carlo method [31]. In a very recent study, Kim et al., report RIXS data from which they fit the magnon dispersion. The conspicuous similarities of the dispersion and the momentum dependence of intensity to those measured in cuprates suggest that the observed mode in RIXS is indeed a single magnon excitation, see Fig. 3.4. Using a phenomenological $J - J' - J''$ model where J, J', and J'' stands for the first, second and third nearest neighbors, respectively, they find $J = 60$, $J' = -20$, and $J'' = 15\,\mathrm{meV}$. The nearest neighbor interaction J is smaller than the theoretical value by roughly 25 %. In addition to the magnon branch, they observe high-energy excitations (0.4 - 0.8 eV) (see Fig. 3.4) which show a strong momentum dependence and are not present in cuprates. This mode is assigned to intra-site excitations of a hole across the spin orbit split levels in the t_{2g} manifold as the energy scale of these excitations coincides with the energy of spin orbit coupling in Sr_2IrO_4.

3.1.3 Experimental Details

Sr_2IrO_4 single crystals with approximate dimensions of $1 \times 0.5 \times 0.5\,mm^3$ are grown by using a flux method by group of Hide Takagi. the crystals are cleaved to establish a virgin, optically flat surface and oriented with Laue diffractometry. A cleaved sample is shown in Fig. 3.5. A later cleaning of these surfaces using acetone or methanol is not advisable due to its deteriorating effect on the sample. Raman spectroscopic studies are performed in quasi-backscattering geometry with a solid-state laser ($\lambda = 532\,nm$ and $4\,mW$ laser power) as excitation light source. The polarizations (xx) and (yx) denote parallel and crossed polarization of incident and scattered light, respectively. $(y'x')$ indicates a rotation of the crystal by 45° along $c-$axis and "u" stands for unpolarized.

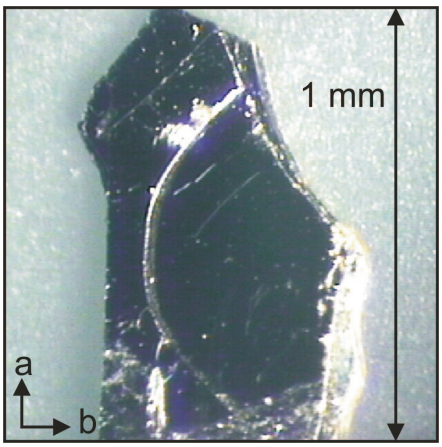

Figure 3.5: A picture of freshly cleaved single crystal of Sr_2IrO_4 taken by a microscope.

Measurements are carried out in an evacuated, closed-cycle cryostat. The spectra are collected via a triple spectrometer (Dilor-XY-500) and a micro Raman setup (Horiba Labram800) equipped with liquid nitrogen cooled charge coupled device (CCD) detector. The measurements of the low (high) energy modes

have been performed with different spectral resolution of 3-4 cm^{-1} and 10 cm^{-1} , respectively, using a slit width of $d = 100$ (250) μm. For resonance Raman investigations different ion gas and solid state Lasers with excitation lines (2.2 - 2.7 eV, 632 - 457 nm) are applied using a power level of $P = 4$ mW. Measurements using a He-Cd Laser (325 nm) have been performed with the micro Raman setup.

3.1.4 Properties of the Phonon Spectrum

Thirty-two Raman active modes are expected according to a factor group analysis [32]. The different ions of Sr_2IrO_4 contribute to all symmetries with the exception of Ir that does not contribute to A_{1g} symmetry, see Table. 3.1.

Table 3.1: Raman active modes according to the factor group analysis for the $I4_1/acd$ structure.

Wyckoff Positions	Raman active modes				Total
Ir (8a)	-	1 B_{1g}	1 B_{2g}	2 E_g	4
Sr (16d)	1 A_{1g}	1 B_{1g}	1 B_{2g}	4 E_g	7
O1 (16d)	1 A_{1g}	1 B_{1g}	1 B_{2g}	4 E_g	7
O2 (16f)	1 A_{1g}	2 B_{1g}	1 B_{2g}	3 E_g	7
O3 (16f)	1 A_{1g}	2 B_{1g}	1 B_{2g}	3 E_g	7

The K_2NiF_4 (I4/mmm) structure yields only four modes, $\Gamma_{Raman} = 2A_{1g} + 2E_g$. In Fig. 3.6 Raman spectra of Sr_2IrO_4 in different polarizations are shown, including in-plane as well as out-of-plane polarizations. In Fig. 3.6(a) six pronounced and four weaker modes are observed, in good agreement with the allowed $4A_{1g} + 7B_{1g}$ modes. For details we refer to 3.2. We detect four out of five expected B_{2g} modes in (yx) polarization. In $(y'x')$ polarization four out of seven B_{1g} modes are observed, see Fig. 3.6(b).

With the incident light polarized parallel to the $c-$axis and no analyzer for the scattered light, denoted by (zu), we detect four of four allowed A_{2g} modes,

Table 3.2: Raman [8] and infrared [26] active modes observed in Sr_2IrO_4.

Freq. (cm^{-1})	Polarization				Assignment	Comments
	xx	yx	y'x'	zu		
82	-	+	-	-	B_{2g} (Ir)	very weak
98	IR				E_u	
138	IR				Sr to IrO_6)	-
187	+	-	-	+	A_{1g} (Sr against IrO_6)	-
252	+	-	-	-	B_{1g} (Sr)	-
270	IR				A_{2u} (Ir-O-Ir bond angle)	softening (2 %)
277	+	-	+	+	A_{1g}(Ir-O-Ir bending)	anomalous softening (6 %)
327	+	-	-	-	A_{1g} (Oxygen)	vanishes at HT
365	IR				A_{2u} (Ir-O-Ir bond angle)	anomalous softening (3 %)
392	+	-	-	+	A_{1g} (Oxygen)	-
395	-	-	+	-	B_{1g} (Ir)	-
399	-	+	-	-	B_{2g} (Sr)	dominating intensity
497	-	+	-	-	B_{2g} (Oxygen)	dominating intensity
560	+	-	+	+	B_{1g}(Oxygen)	asymmetric line shape
660	IR				A_{2u}(Ir-O bond)	broadening, softening
666	+	-	-	-	B_{1g} (Oxygen)	very weak
690	+	-	+	-	B_{1g} (Oxygen)	-
706	-	+	-	-	B_{2g} (Oxygen)	-
728	+	-	-	-	B_{1g} (Oxygen, breathing)	anomalous broadening
850	+	-	-	-	B_{1g} (Oxygen)	very broad, asymmetric line shape
1240	+	-	-	-	2-Phonon of 666 cm^{-1}	-
1345	+	-	-	-	2-Phonon of 690 cm^{-1}	-
1467	+	-	-	-	2-Phonon of 728 cm^{-1}	dominating with low energy Lasers
1800	+	-	-	-	2-Magnon / electronic	large linewidth, vanishing at HT

see Fig. 3.6(c). We detect none of the sixteen E_g modes in crossed polarization. This could be attributed to their small scattering cross section. It is obvious from these data that in each polarization a different mode has a dominating intensity, i.e. at 277 cm^{-1}, 399 $cm^{-1}$and 560 cm^{-1} modes in (xx), (yx) and (zu) polarizations, respectively. This is evidence for a pronounced spatial anisotropic polarizability as expected for a layered material. A mode assignment based on the mode frequency and a comparison with earlier data from IR experiments [26, 27] is given in Table 3.2.

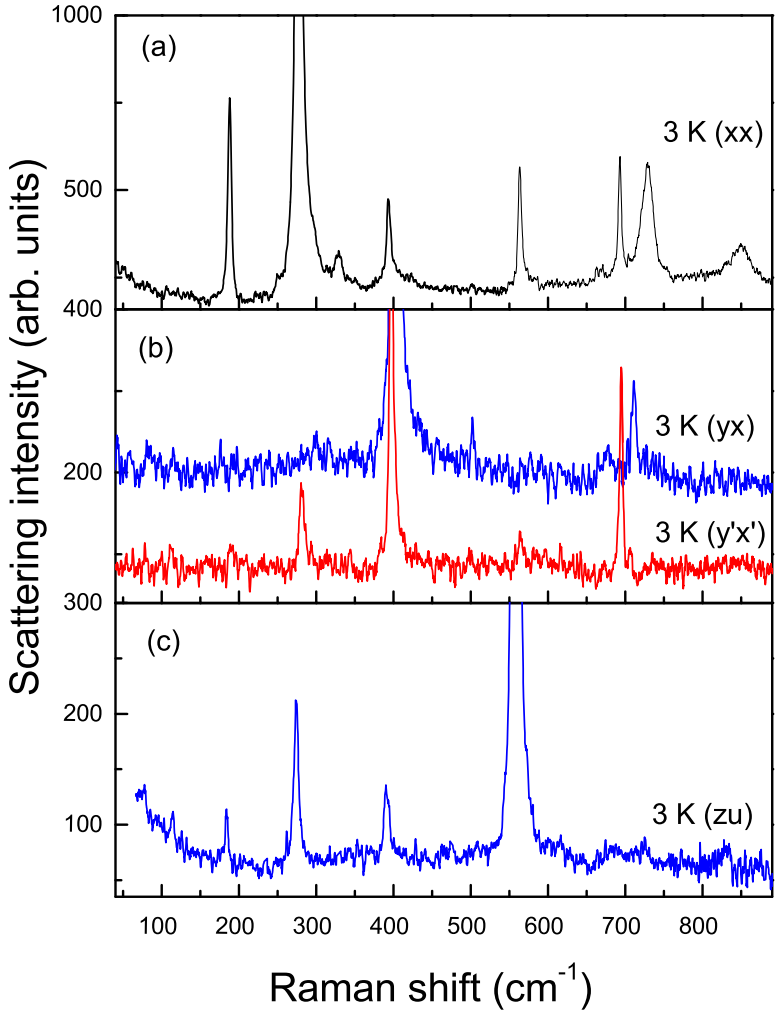

Figure 3.6: Polarization dependence of the Raman spectra measured at 3 K in (xx) polarization (a), (yx) and $(y'x')$ polarizations (b), and (zu) polarization (c) [8].

A comparison of spectra at two temperatures within the low, medium and high spectral ranges is depicted in Fig.3.7(a), (b) and (c), respectively. All observed phonons increase in intensity and get sharper in line shape at low temperatures. The lower energy A_{1g} modes, 187 cm^{-1} and 277 cm^{-1}, can be assigned to Sr stretching against IrO_6 and the bending mode of the Ir-O-Ir bonds, respectively [33, 34]. Weak modes at 252 cm^{-1} and 327 cm^{-1} vanish at high temperature. Breathing modes of apical oxygen showing up in the frequency range of 500 cm^{-1} to 850 cm^{-1} are asymmetric and have Fano-like line shapes. This is probably related to an interaction with a continuum of excitations.

In the higher frequency range we observe additional maxima in the scattering intensity. These modes at around 1240 cm^{-1}, 1345 cm^{-1} and 1467 cm^{-1} have a very large linewidth (50 cm^{-1}) and look more like density of states than usual phonon modes. Therefore we assign them to 2-phonon scattering of the 666 cm^{-1}, 690 cm^{-1} and 728 cm^{-1} phonon modes, respectively. The observation of 2-phonon scattering with large intensity resembles to observations in correlated $3d$ electron systems with orbital dynamics [35, 36, 37, 38].

The normalized intensity, linewidth (FWHM) and frequency of particular modes which behave anomalously are depicted in Fig. 3.8. All modes display a general increase in intensity and a decrease in linewidth as temperature decreases. The phonon at 277 cm^{-1} shows an anomalously large shift (20 cm^{-1} $\approx$ 6 %). It is assigned to a modulation of the Ir-O-Ir bond angle. The linewidth of the mode at 728 cm^{-1} shows a kink at approximately 100 K. For temperatures above 100 K, its linewidth broadens substantially and saturates for $T > T_N = 240$ K. Frequency and intensity of the phonon at 728 cm^{-1} and its 2-phonon mode (at 1467 cm^{-1}) behave similarly with increasing temperatures. We have performed fits to the

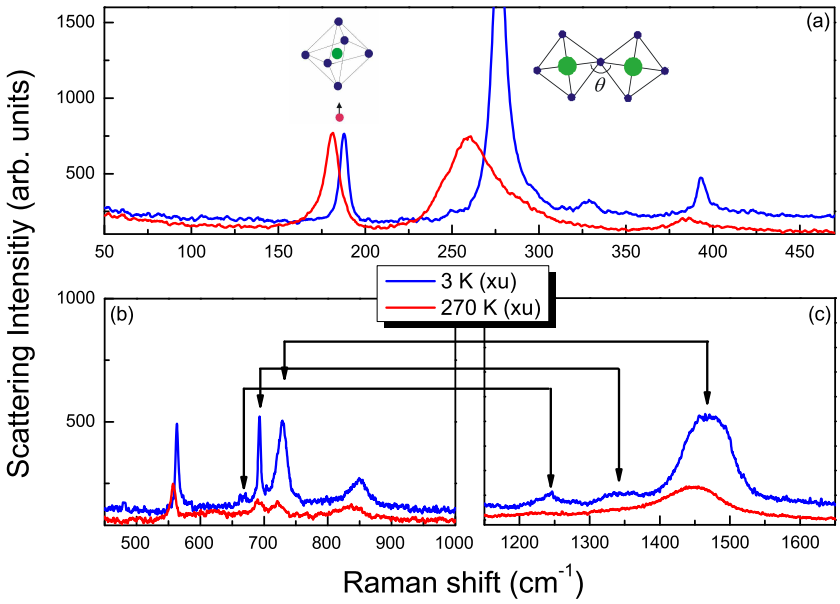

Figure 3.7: Comparison of Raman spectra at 3 K (blue) and at 270 K (red) in the (a) low, (b) medium, and (c) high energy spectral ranges in (xu) light scattering polarization. Displacement patterns in (a) correspond to the A_{1g} mode at 187 cm^{-1} (Sr vs. IrO_6) and the A_{1g} mode at 277 cm^{-1} (Ir-O-Ir bond angle modulation) [8].

mode frequencies according to the Grüneisen's Law (Eq. 3.1) with temperature dependent unit cell volumes [20]. The resulting parameters γ values are larger than expected for usual anharmonicity ($\gamma_{usual} \approx 2$). This evidences strong anharmonicity of the particular modes due to coupling to electronic degrees of freedom.

$$\frac{\Delta\omega_i(T)}{\omega_i(290)} = -\gamma_i \frac{\Delta V_0(T)}{V_0(290)} \tag{3.1}$$

All phonons show an increase of intensity with decreasing temperature. We assign this seemingly trivial effect to the changing optical penetration depth and scattering volume. The optical (Mott-Hubbard) gap in Sr_2IrO_4 is small and the states in the gap contributing to the optical conductivity and penetration depth are only gradually depleted with decreasing temperature. More specific and larger

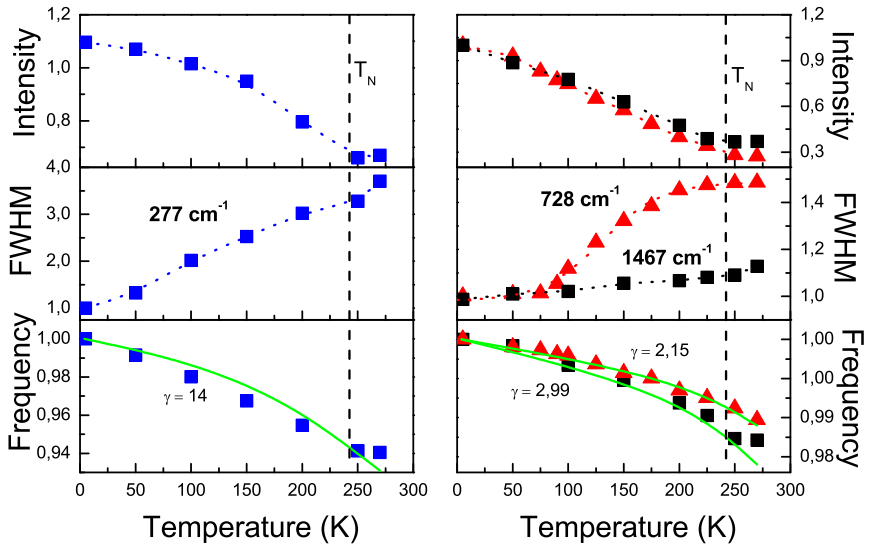

Figure 3.8: Temperature dependence of the normalized integrated intensities, linewidth (FWHM) and peak positions of the phonon modes at 277, 728, and the 2-phonon mode at 1467 cm^{-1}. Dotted lines are guide to the eye. Solid green lines are the fits according to a Grüneisen's law with given Grüneisen parameters γ [8].

anomalies concern modes that are related to Ir - O bending and stretching modes. In general these anomalies are noteworthy, as due to their low energy the O2p states only weakly hybridize with Ir 4*d* states. Therefore one expects small related spin phonon coupling constants. In contrast, the observed anomalies are rather strong, see, e.g. the 6-7 % softening of the 277 cm^{-1} mode. Therefore we have to assign them to different coupling mechanisms. The gradual evolution of the phonon frequencies and only moderate changes at the ordering temperature point to a phonon coupling to the SOC induced gap itself. As the magnitude of the gap is due to an interplay of SOC with correlations the dependence of SOC on local symmetry leads to an effective electron-phonon coupling mechanism. This is in agreement with Table 3.2 where phonons related to the Ir - O bonding angle and length show appreciable anomalies without being very specific. Therefore, the

linewidth of these modes and the intensity of multiphonon scattering is not dominated by conventional anharmonicity via phonon scattering but by excitations of the isospin manifold of states. The abrupt change of the multiphonon lineshape with excitation energy shown in the inset of Fig. 3.11 is thereby taken as an indication of the entanglement of structural and electronic degrees of freedom in this compound.

3.1.5 High Energy Excitations

We observe another very broad maximum (width $1000\,\mathrm{cm}^{-1}$) at low temperatures and centered at higher energy ($1800\,\mathrm{cm}^{-1}$), see Fig. 3.9. This maximum is a candidate for two spin excitations as the corresponding branches in RIXS have been observed with typical energies at 800 and $1600\,\mathrm{cm}^{-1}$ in dependence of wave vector and a similar large dispersion [3]. It should be noted, however, that despite similarities of the $J_{eff} = 1/2$ to a $s = 1/2$ quantum spin system the dynamics of the former state can be very different. This concerns the energy, lineshape and temperature dependence of two particle processes and has its origin in the different dependence of isospin exchange processes on additional orbital and geometric factors. To our knowledge no experimental or theoretical investigation of isospin excitations in Raman scattering exists.

From Fig. 3.9 we also deduce a strong suppression of the integrated scattering intensity with increasing temperatures and its vanishing at approximately 250 K. Such a temperature induced suppression is not observed for $s = 1/2$ two-magnon scattering even for $T \approx T_N$. Two magnon scattering is based on a local spin exchange and their characteristic energies depend only weakly on long range

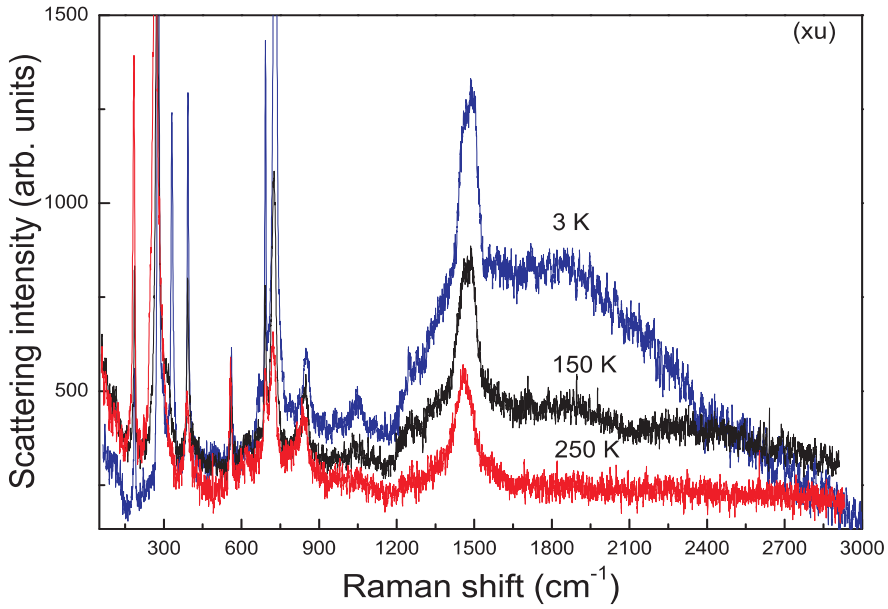

Figure 3.9: 2-Magnon scattering in Sr_2IrO_4. The measurements are performed in (xu) polarization with a 561 nm excitation at T = 3 K, 150 K, and 250 K [8].

ordering.

Similar as the resonant intensity of phonon modes also magnetic and electronic Raman scattering are rather sharp markers of the correlated electron energy scales. Prominent examples are the parent compounds of HTSC that show two magnon scattering at approximately *3J*, with J the exchange coupling, [39], and the spin liquid state on the Kagome lattice with a broad response distributed from zero energy to at least *5-6 J* [40]. Also in Sr_2IrO_4 the broad asymmetric feature centered at around 1800 cm^{-1} ($\approx$ 0.23 eV) is attributed to magnetic Raman scattering. This position corresponds to an exchange coupling $J = 850$ K ($\sim$ 74 meV). Here we use a 2D bond model with 4 nearest neighbors and a spin of 1/2, i.e. $E_{max} = J(2zs\text{-}1)$. This energy lies a bit below the range of earlier estimations of $J = 1000$ K [31].

There are several properties that are uncommon compared to two magnon

scattering. All of them speak individually for an interaction of the spin system with other degrees of freedom. The normalized linewidth of approximately $1000\,\mathrm{cm}^{-1}$ ($\mathrm{w} = \mathrm{E}/\mathrm{E}_{max} = 0.55$) is very large compared to NiF_2, a canted AF, ($\mathrm{w} = 0.076$) [41] and still larger than in the parent compounds of high temperature superconductors ($\mathrm{w} = 0.37$) [39]. It is, however, quite similar to the width ($0.11\,\mathrm{eV} \approx 900\,\mathrm{cm}^{-1}$) of the resonance profile at 2.5 eV given in Fig. 3.10. This similarity can evidence a decay of the magnon scattering via charge excitations. The magnetic scattering intensity in Sr_2IrO_4 is rapidly depressed with increasing temperatures. This temperature dependence is paralleled by the spectral weight shift in optics and is not expected in a conventional system without orbital degrees of freedom.

3.1.6 Resonance Effect

In Sr_2IrO_4 as well as other oxide based correlated electron systems the weakly hybridized states of the transition metal oxide coordinations form narrow bands with a highly structured density of states. If these energy scales fit to the photon energies of incident Laser radiation resonance Raman Scattering (RRS) can be observed. It is noteworthy that the Raman excitations process couples the induced electron hole pair exactly to the states that are relevant for magnetism and for spin phonon coupling and can give intriguing information. Such experiments on two magnon states have supported the Hubbard model description of high temperature superconductors [39].

In Fig. 3.10(a) we show the dependence of selected phonon intensities ($187\,\mathrm{cm}^{-1}$, $277\,\mathrm{cm}^{-1}$) and the 2-phonon ($1467\,\mathrm{cm}^{-1}$) intensity on the incident laser energy.

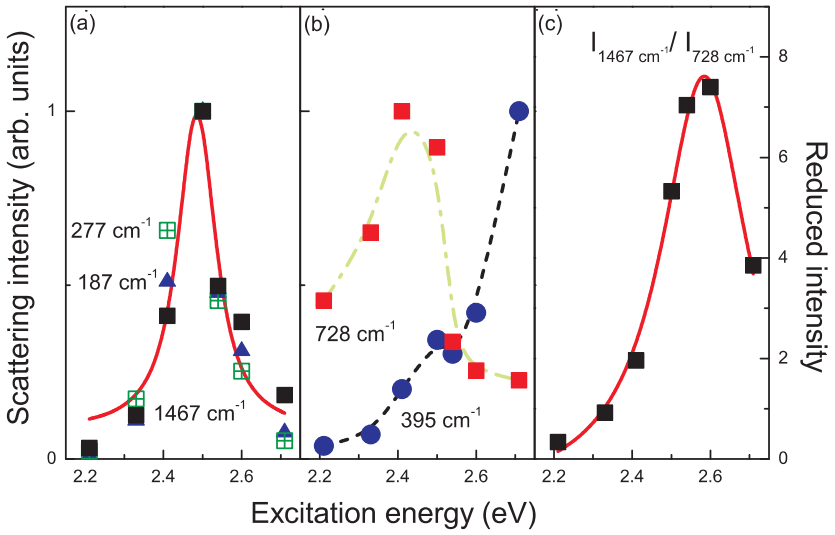

Figure 3.10: Intensity of phonon Raman scattering as function of Laser excitation energy. (a) Phonon intensity at 187 cm^{-1}, 277 cm^{-1}, and the 2-phonon intensity at 1467 cm^{-1}; (b) Phonon intensity at 395 cm^{-1} and 728 cm^{-1}; (c) intensity ratio of 2-phonon (1467 cm^{-1}) to 1-phonon scattering (728 cm^{-1}). The solid red line is a fit to a Lorentzian line shape [8].

There exist a very sharp maximum at 2.5 eV. This characteristic energy is also known from RIXS and IR absorption. For the mode at 728 cm^{-1} and 395 cm^{-1} there is a broader profile and a resonance to higher energies, respectively, see Fig. 3.10 (b). This is attributed to different electronic states relevant for these phonon modes. Furthermore, also the intensity ratio of the 2-phonon to the 1-phonon modes shows a maximum at 2.58 eV, see Fig. 3.10(c). This is evidence that the enhanced intensity of 2-phonon scattering is also related to a resonant scattering process. For HTSC and manganites such pronounced resonances of phonon scattering intensities have not been observed.

The phonon intensities in Fig. 3.10 show two resonance energies at 2.5 eV and above 3 eV, that belong to the same charge transfer excitation of the weakly dispersing isospin state [25]. In optics the respective spectral range shows a

shift of spectral weight from around 0.5 eV to higher energies with decreasing temperatures [26, 27]. The lower energy regime corresponds most probably to excitations across the Hubbard bands that form the optical gap. This spectral weight shift is very likely the origin for most of the phonon anomalies as function of temperature shown in Fig. 3.8. As the phonon frequency is also affected by other electronic states these anomalies are less pronounced.

3.1.7 Crossover Phenomenon

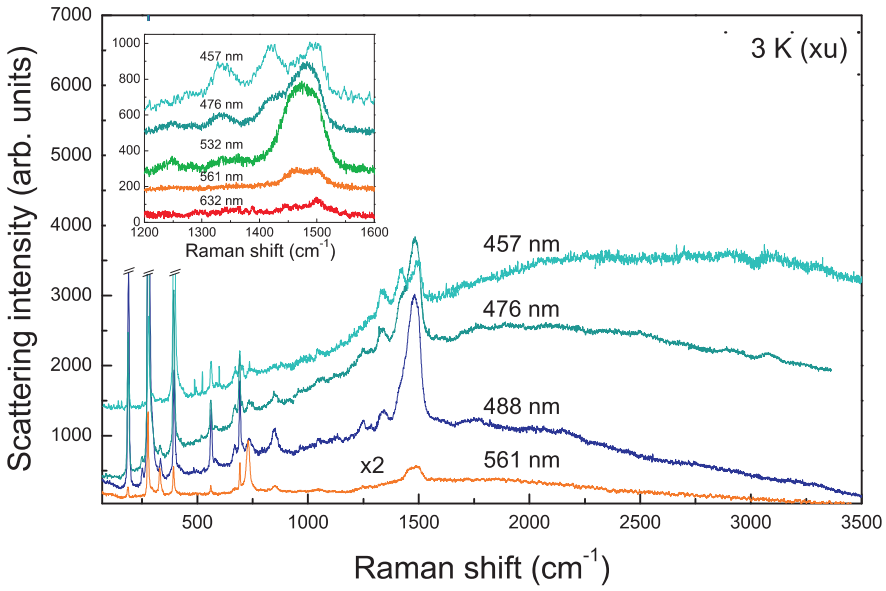

Figure 3.11: Resonance Raman spectra with increasing excitation energy at T = 3 K in (xu) polarization. The inset shows the frequency regime of two phonon scattering with increasing excitation energy from 632 nm to 457 nm, from bottom to top. These curves are shifted for clarity [8].

Increasing the Laser energy above 2.6 eV ≈ 476 nm the broad Raman mode is replaced by an even broader background that seemingly shifts to higher energies, see Fig. 3.11. In contrast to the former Raman process attributed to a two particle excitation of coherent (magnon-like) excitations the mode observed with

higher energy is incoherent and shifts only on the relative scale "Raman shift". In the inset of Fig. 3.12 this signal is plotted on an absolute energy scale. We find a negligible frequency shift as function of the incident Laser energy. The onset of the second process is around 2.55 eV, an energy which is again related to the characteristic resonance in Sr_2IrO_4. As in previous RIXS experiments [3] this energy has been related to the creation of excitons in the $J_{eff} = 1/2$ to 3/2 isospin level manifold, we denote this regime *exciton regime*.

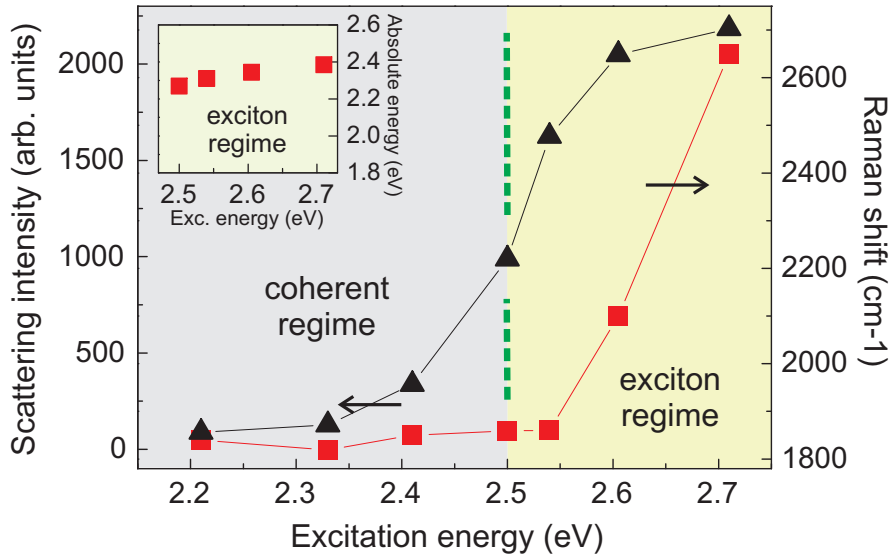

Figure 3.12: Intensity and Raman shift of the broad high energy mode that is observed in Sr_2IrO_4 as function of Laser excitation energy. The dashed line marks the crossover from a coherent regime to an exciton regime. Inset: In the exciton regime the absolute energy of this mode does only weakly depend on excitation energy [8].

In the exciton regime there is also a drastic change of the 2 phonon line-shape evident around 1500 cm^{-1}, see inset of Fig. 3.11. With lower excitation energy only a single, hump-like mode is observed. Such a line shape origins from multiparticle scattering with no preferred scattering vector. With higher energy this signal is strongly enhanced and splits into a sequence of peaks. Its

lineshape is rather similar to observations in manganites [35, 36, 37] or TiOCl [38] with orbital ordering and incommensurate distortions. In TiOCl the 2 phonon scattering evolves at the lower boundary of the energy scale of two-particle electronic/magnetic scattering. A similar coincidence of energy scales exists in Sr_2IrO_4. The main difference between the $3d$ and the $5d$ compound, however, is the control of scattering lineshape and intensity by the excitation energy of the scattering process. In $3d$ compounds a crossover does not exit.

The suppression of the two-magnon scattering with increasing excitation energy and crossover to an incoherent broad signal is rather special. This crossover is attributed to the proximity of the spin excitations to charge modes at the top of the Mott-Hubbard gap. This intermixing in the exciton regime is a direct consequence of the dominating spin-orbit coupling. In contrast to the sharp resonance of the phonon modes, the maximum in the incoherent exciton regime is extremely broad. This could be due to metastable electronic configurations like a spin/charge polarons that are induced by the optical absorption process with energies above the resonance, i.e. threshold energy. The formation of polarons has been shown to induce resonant Raman scattering, e.g. in the double perovskite Ba_2MnWO_6 [42]. However there are also other candidates as long living topological excitations or solitons [43].

3.1.8 Summary

Resonance Raman scattering data of the SOC dominated Mott insulator Sr_2IrO_4 shows a rather sharp resonance of the phonon intensity at 2.5 eV and other anomalies due to an O2p - Ir t_{2g} charge transfer excitation across the Mott-Hubbard

gap. The observed temperature dependence is attributed to a spectral weight shift induced by the lowest electronic levels in the optical gap. With a Laser excitation energy above the resonant threshold energy of 2.5 eV the magnon scattering crosses over to a broad incoherent scattering contribution. We attribute this to a coupling to charge modes and the formation of an exciton regime. The presented data demonstrate an interesting case of a correlated electron system dominated by spin-orbit coupling.

3.2 The Bilayered Perovskite $Sr_3Ir_2O_7$

3.2.1 Crystal Structure

$Sr_3Ir_2O_7$ belongs to Ruddlesden-Popper series and has tetragonal unit cell with I4/mmm space group (No. 139) and Z = 2 [45]. The crystal structure is solved by means of single crystal X-ray diffraction. The structural refinement shows that the IrO_6 octahedra are rotated about the $c-$axis by about 12°, similar to the rotational distortion found in Sr_2IrO_4. However, unlike in Sr_2IrO_4, the IrO_6 rotations in $Sr_3Ir_2O_7$ are not correlated, hence no superlattice reflections appear [46]. The structure of $Sr_3Ir_2O_7$ consists of strongly coupled double Ir-O layers, separated by layers of Sr-O along c-axis [47] as it is depicted in Fig. 3.13.

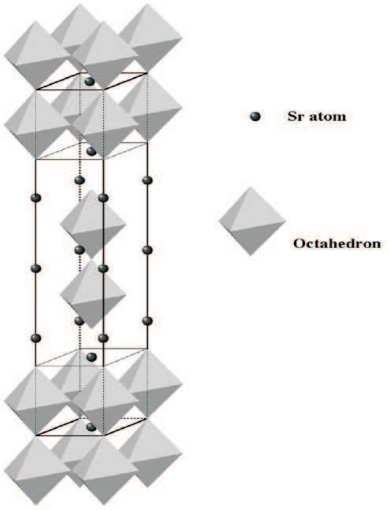

Figure 3.13: Crystal structure of $Sr_3Ir_2O_7$ [44].

3.2.2 Electronic and Magnetic Properties

$Sr_3Ir_2O_7$ is an interesting 5d system in which an insulating ground state similar to Sr_2IrO_4 is observed [48, 49, 50]. Moon et al. study various 5d systems to see if it is possible to have an insulator-metal transition by systematically changing the bandwidth W. W should be proportional to the number of neighboring Ir

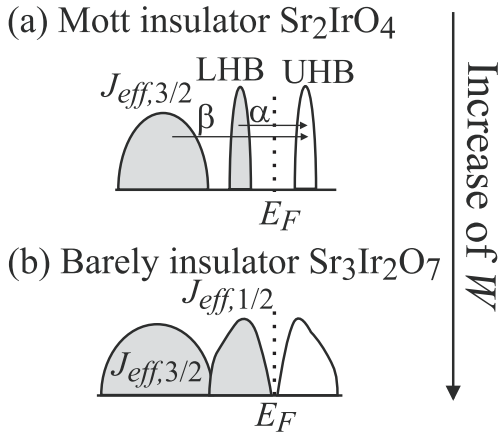

Figure 3.14: Schematic band diagrams of Sr_2IrO_4 (a) and $Sr_3Ir_2O_7$ (b) in which band structure is shaped by strong spin orbit coupling [49].

atoms z, therefore, W is expected to be larger in $Sr_3Ir_2O_7$ ($z = 5$) than it is in Sr_2IrO_4 ($z = 4$), see Fig. 3.14. First principle calculations and optical spectroscopy experiments show that the W of $5d$ bands, indeed, increases with dimensionality or the z value [49]. An insulator-metal transition is observed in optical conductivity spectrum (see Fig. 3.15) when the z value is increased. Sr_2IrO_4 demonstrates a finite-sized optical gap, Fig. 3.15 (a), and this gap is suppressed and becomes almost zero for $Sr_3Ir_2O_7$ (Fig. 3.15) (b). The peak α is attributed to an optical transition from the lower Hubbard band to the upper Hubbard band of $J_{eff} = 1/2$ states while peak β is due to the transition from the $J_{eff} = 3/2$ bands to the upper Hubbard band. These peaks shift to lower energy as the z value, i.e. W increases. A reason for this shift is discussed to be a result of the increase of the spectral weight in the gap region, which would fill the Mott gap with larger W. Therefore, higher z number, i.e., higher number of Ir ions along c-axis yields stronger hybridization of d bands through the apical O ions [49]. In the light of this information one would expect stronger electron phonon coupling for the modes in which apical oxygen is involved. This effect

may show up as phonon anomalies, i.e. big frequency shifts and anharmonicity, in Raman spectra.

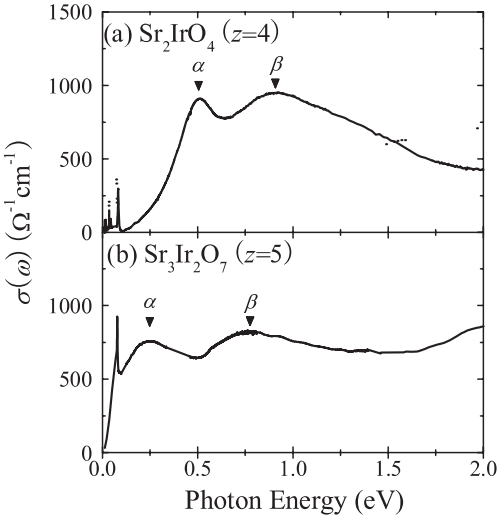

Figure 3.15: Optical conductivity spectra $\sigma(\omega)$ of Sr_2IrO_4 (a) and $Sr_3Ir_2O_7$ (b) [49].

There are several reports about the magnetic structure of $Sr_3Ir_2O_7$ [30, 47, 51, 52, 53]. It is shown that $Sr_3Ir_2O_7$ is a magnetic insulator with a transition to weak ferromagnetism at $T_C = 285\,\mathrm{K}$ [51]. The magnetic moment at low temperatures (2-7 K) is measured to be less than 4 % of the moment expected for a localized spin $S = 1/2$, i.e., $0.037\mu_B$/Ir. Fig. 3.16 demonstrates the magnetization for the basal plane and the c-axis as a function of temperature for various external magnetic fields (0.01, 0.05, 0.1, 0.25, 0.5, and 7 T). Field cooled magnetization shows a sudden ferromagnetic transition at $T = 285\,\mathrm{K}$. Most surprisingly the field cooled magnetitzation starts decreasing rapidly below $T_D = 50\,\mathrm{K}$ and peculiarly becomes negative at $T < 20\,\mathrm{K}$. This may be due to a magnetization reversal or a rotation of the magnetic moment that orients opposite to the magnetic field. μSR measurements also detect an anomaly for the same temperature, $T < 20\,\mathrm{K}$.

Franke et al. report oscillations of the muon decay asymmetry for $Sr_3Ir_2O_7$ which is a signiture of magnetic ordering disappear for $T < 20\,\mathrm{K}$. Frequency reversal of magnetization has been observed also in ferrimagnetic spinels such as Co_2VO_4 and Co_2TiO_4 in which two inequivalent magnetic sublattices are antiferromagnetically coupled [54]. The origin of magnetization reversal in these compounds is

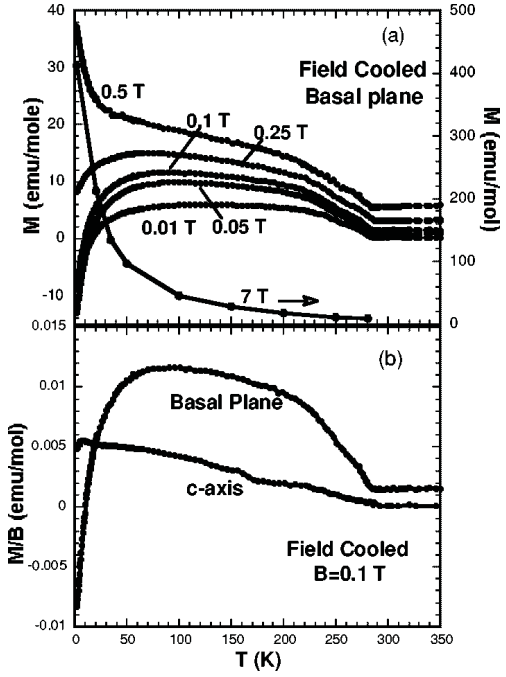

Figure 3.16: Magnetization for basal plane and $c-$axis of $Sr_3Ir_2O_7$ [51].

believed to be a different temperature dependence of individual magnetic sublattices. However, unlike the ferrimagnetic spinels, $Sr_3Ir_2O_7$ has no two inequivalent magnetic sublattices. A change of orbital ordering and reversed Dzyaloshinskii vector induced by enhanced SOC is discussed to be the reason for the reversal of magnetization in vanadates ($LaVO_3$ and YVO_3) [55, 56]. Even though Cao et al. claim that the orbital angular momentum and SOC (SOC quenches due to the crystalline fields) can not be the reason for the reversal of magnetization,

more recent studies have shown that SOC is significantly large also in $Sr_3Ir_2O_7$ [49]. Therefore, it is believed that interplay of SOC with temperature dependent rotational distortions can be the answer to the reversal of magnetization in $Sr_3Ir_2O_7$. These anomalies could not be observed in zero field cooled measurements, which is attributed to a strong spin disordering or a random orientation of magnetic domains that is persistent through T_C [51]. It is noteworthy that the magnetization shows a pronounced upturn at low temperatures and becomes stronger with higher fields B. For $B = 7\,\mathrm{T}$, $Sr_3Ir_2O_7$ behaves more like a paramagnet. Moreover, field cooled magnetization curves for the basal plane and the c-axis point out a strong magnetocrystalline anisotropy. Fig. 3.16(b) shows that the easy axis for magnetization obviously lies within the basal (ab) plane. The magnetic anisotropy between the a and the b is negligible [51]. In Fig. 3.17, the

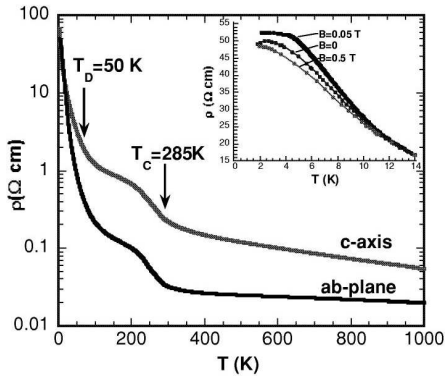

Figure 3.17: Resistivity $Sr_3Ir_2O_7$ as a function of temperature [51].

electrical resistivity $\rho(T)$ as a function of T for the basal plane and c-axis in the temperature range from 1.5 K up to 1000 K is shown [51]. ρ shows a steep increase at 285 K and around 50 K as the temperature decreases. These two temperatures are where the magnetization shows anomalies as well, indicating the coupling of magnetic and transport behaviors [51]. ρ_{ab} is fit with $1/T^{1/4}$ for $15< T <100\,\mathrm{K}$

which is attributed to a variable range hoping with negligible Coulomb interaction. The origin of variable range hoping is explained by localization of states close to the band edges which is discussed to be due to a distribution of rotation angles as it is likely that the rotation of octahedra is not uniform throughout the crystal [51].

3.2.3 Experimental Details

Polycrystalline samples of $Sr_3Ir_2O_7$ are grown by using a flux method by the group of Chengtian Lin at MPI-FKF Stuttgart. Polycrystalline pellets are cleaved to establish a virgin, optically flat surface. Measurements are carried out on the microcrystals found in the cleaved polycrystalline pellets shown in Fig. 3.18. Unfortunately, the crystal orientation with Laue diffractometry is not possible because of the very small crystal size. However, the shiny plane shown in Fig. 3.18 is assigned to be the *ab* plane as the polarized Raman spectra. This is consistent with the calculated number of modes according to the factor group analysis. Raman spectroscopic studies are performed in quasi-backscattering geometry in *ab*-plane with a solid-state laser ($\lambda = 532\,\mathrm{nm}$ and $1.8\,\mathrm{mW}$ laser power) as excitation light source.

Measurements are carried out in an evacuated, liquid He cooled cryostat. The spectra are collected via a micro Raman setup (Horiba Labram) equipped with a liquid nitrogen cooled charge coupled device detector. The measurements have been performed with spectral resolution of 3-4 cm^{-1} using a slit width of $d = 100\,\mu\mathrm{m}$. A detailed Resonance Raman investigation could not be performed as the micro Raman setup is equipped with only a solid state Nd:YAG laser

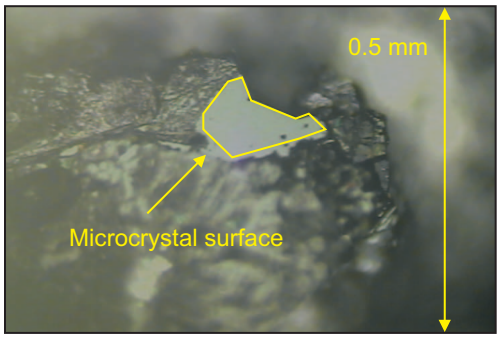

Figure 3.18: A picture of a freshly cleaved polycrystalline pellet of $Sr_3Ir_2O_7$ taken by a microscope.

(λ =532 nm) and He-Ne (λ =632.8 nm) laser.

3.2.4 Properties of the Phonon Spectrum

Factor group analysis yields 14 Raman active modes for $Sr_3Ir_2O_7$ with space group $I4/mmm$. The corresponding symmetries are given in Table 3.3.

Table 3.3: Raman active modes according to the factor group analysis for the $I4/mmm$ structure.

Wyckoff Positions	Raman active modes				Total
Ir (4e)	1 A_{1g}	-	-	1 E_g	2
Sr1 (2b)	-	-	-	-	0
Sr2 (4e)	1 A_{1g}	-	-	1 E_g	2
O1 (2a)	-	-	-	-	0
O2 (4e)	1 A_{1g}	-	-	1 E_g	2
O3 (16n)	1 A_{1g}	2 B_{1g}	1 B_{2g}	3 E_g	8

Fig. 3.19 shows Raman spectra of $Sr_3Ir_2O_7$ in different polarizations at 5 K. In parallel polarization of incident light to scattered light, (xx), 4 very sharp and intense modes (147, 182, 285, and 592 cm^{-1}) were observed. In addition to those modes, 3 weak and broader modes (399, 677, and 732 cm^{-1}) were recorded. The number of observed modes in (xx) polarization is in very good agreement

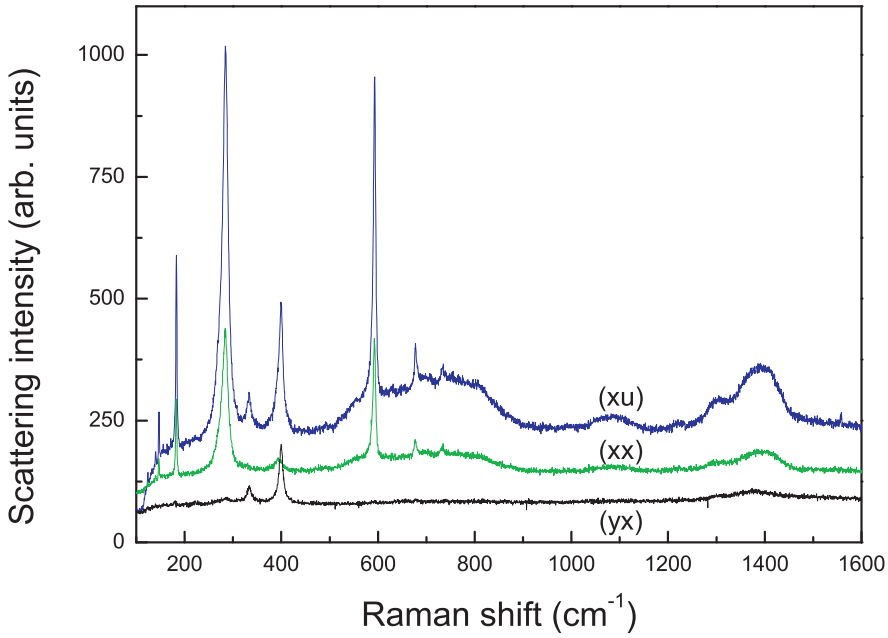

Figure 3.19: Raman spectra of $Sr_3Ir_2O_7$ recorded in different polarization geometries and at 5 K. Spectra are shifted vertically for clarity.

with the number of expected modes ($5A_{1g}$+$2B_{1g}$) in this polarization. In the measurements without analyzer (xu) phonon intensities are much higher and an an extra mode shows up at 333 cm^{-1} which might be leaking of a not allowed mode. In crossed polarization of incident light to scattered light (yx), 7 modes ($1B_{2g}$ + $6E_g$) are expected. However, only 2 modes (333 and 399 cm^{-1}) were observed. This might be due to low scattering intensity because of small scattering cross section. The broad continuum centered at 700 cm^{-1} and DOS like features at around 1300 and 1400 cm^{-1} which were observed in (xu) polarization, were quite suppressed in (xx) polarization and totally disappeared in crossed polarization. We believe that this broad continuum centered at 700 cm^{-1} has its origin in mixed electronic and magnetic scattering, as discussed later. The additional high energy maxmima, have very large linewidth (50 cm^{-1}) compared to the sharp

phonon peaks. Therefore we assign them to 2-phonon scattering of the 677 and 732 cm^{-1} phonon modes, respectively. The observation of 2-phonon scattering with large intensity resembles to observations in correlated $3d$ electron systems with orbital dynamics [35, 36]. In Fig. 3.20, Raman spectra recorded at high

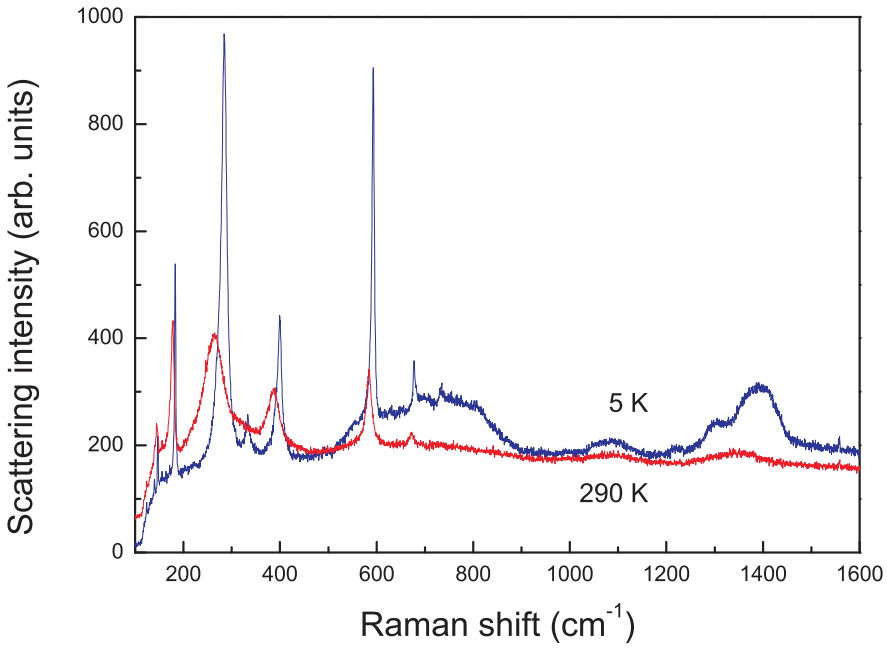

Figure 3.20: Raman spectra of $Sr_3Ir_2O_7$ recorded at high (290 K) and low (5 K) temperatures in (xu) polarization.

(290 K) and low (5 K) temperatures in (xu) polarization are shown. All observed phonons increase in intensity and get sharper in line shape at low temperatures. Similar to the phonons in Sr_2IrO_4, lower energy modes 147 and 182 cm^{-1} can be assigned to Sr stretching against IrO_6 while the mode at 285 cm^{-1} can be attributed to the bending mode of Ir-O-Ir bond. Modes at higher energies (592 and 677 cm^{-1}) which are superimposed by a broad continuum, lose intensity at high temperature and the mode at 732 cm^{-1} disappears at high temperature.

Phonon frequencies observed in (xu) polarization as a function of temperature

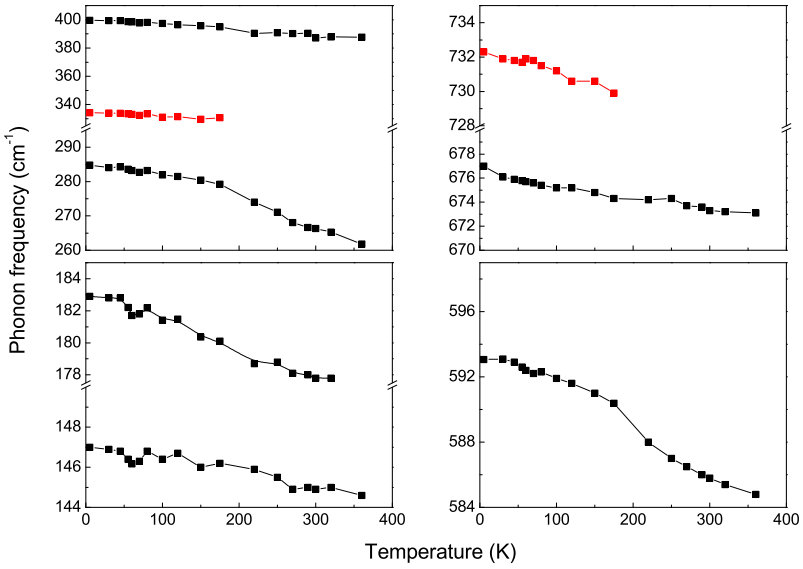

Figure 3.21: Phonon frequencies of $Sr_3Ir_2O_7$ as a function of temperature.

are shown in Fig. 3.21. All phonons show a hardening for decreasing temperatures. Two additional modes (333 and 733 cm^{-1}) show up at lowest temperature, however they decrease in intensity for increasing temperatures and finally disappear at temperature above 200 K which is way below the magnetic transition temperature (285 K). This is a hint for slight structural changes/distortions showing up below a certain temperature. As these particular phonons are attributed to magnetic Ir atoms, magnetic interactions might be enhancing these modes below the magnetic transition temperature. The reason that they do not persist up to the magnetic transition temperature (285 K) could be that imperfections in the magnetic structure or the changes in the bond angle due to the temperature.

Some other phonon anomalies similar to the Sr_2IrO_4 are observed, i.e. the mode at 287 cm^{-1} shows an anomalous shift (27 cm^{-1} $\sim$ 9%). This mode is attributed to the bending of the Ir-O-Ir bond analogously to the Sr_2IrO_4. However,

in Sr_2IrO_4 it has a slightly lower energy ($277\,cm^{-1}$). This might be due to the small difference between the tilting angles of IrO_6 octahedras in these two compounds. Moreover, the bigger shift of the mode in $Sr_3Ir_2O_7$ indicates that the buckling angle of the Ir-O-Ir bond is more sensitive to the temperature for this compound than it is for the Sr_2IrO_4 as the structures of the two compounds are not totally identical.

The low frequency modes (147 and $183\,cm^{-1}$) and the mode at $592\,cm^{-1}$ show some instabilities in frequency at around 50 K . At this temperature the magnetization is showing a downturn [51]. Therefore, one could suggest that these modes are interacting with the magnetic spins and effected by a change in the magnetic structure of the compound. Strong spin orbit coupling might be the driving force for these interactions between spins and lattice vibrations.

3.2.5 Broad Modes in the Raman Spectrum of $Sr_3Ir_2O_7$

The temperature evolution of the broad features observed at around 700 and $1400\,cm^{-1}$ is depicted in Fig. 3.23. Spectra are phonon subtracted for clarity. The lower energy mode at around $700\,cm^{-1}$ consists of two components centered at around 584 (A) and $750\,cm^{-1}$ (B). The higher energy mode also has a shoulder centered at $1300\,cm^{-1}$(C). These modes are rather broad (linewidth $\sim$80 cm^{-1}) compared to phonon modes and seem to be more like density of states. Lower energy components of both modes (A and C) are relatively weaker and at temperature above 120 K, they merge together with higher energy components (B and D). This temperature surprisingly does not correlate with any known transition temperature. Moreover, these modes persist up to 360 K which is way above the

magnetic ordering temperature (285 K).

Even though $Sr_3Ir_2O_7$ and Sr_2IrO_4 have a very similar crystal structure, the magnetic excitation spectra of both compounds are significantly different (see Fig. 3.9), pointing out a very different magnetic structure. Recently Kim et al. have reported the magnetic structure of $Sr_3Ir_2O_7$ based on XRD measurements [4**?**]. They find an AF structure with $c-$axis collinear moments in $Sr_3Ir_2O_7$, in contrast to the $ab-$plane canted AF found in Sr_2IrO_4. Kim et al. also claimed that the observed two-magnon transition as a function of number of IrO_2 layers does not accompany an orbital reconstruction, which shows that the strong inter-layer couplings, supported by the three dimensional shape of the $J_{eff} = 1/2$ wavefunction, are indeed responsible for the spin-flop transition [**?**]. In bilayer $Sr_3Ir_2O_7$ strong inter-layer couplings are expected since the spin-orbit entangled wavefunction in iridates is of 3D character [24].

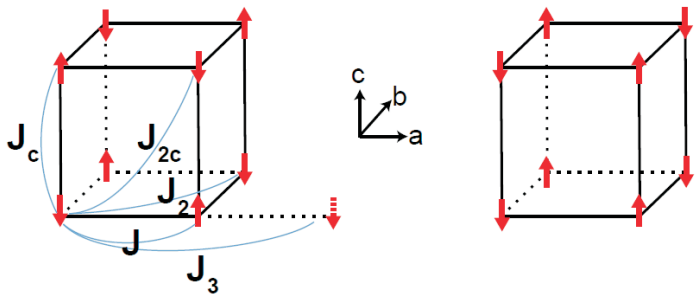

J	J_c	J_2	J_3	J_{2c}
93	25.2	11.9	14.6	6.16

Figure 3.22: Coupling constants for $Sr_3Ir_2O_7$ (in units of meV) extracted from the fits to the experimental magnon dispersion in RIXS measurements [4].

Magnetic coupling constants (J), in units of meV, determined from fits to the experimental magnon dispersion curves are shown in Fig. 3.22 [4]. The energy of

two magnon scattering can be estimated using a 2D bond model with 4 nearest neighbors (z) and a spin of s=1/2, i.e. E_{max}=J(2zs-1). The position of the lower energy broad features (A+B $\sim$ 700 cm^{-1}) corresponds to an exchange coupling $J \sim 28$ meV. This value is in a good agreement with the inter-layer coupling constant (J_c) determined by RIXS measurements (see Fig. 3.22) which suggest that this broad feature might be due to a double spin flop scattering along the $c-$axis in the bilayer $Sr_3Ir_2O_7$. The higher energy modes (C+D $\sim$ 1400 cm^{-1}) correspond to an exchange coupling of $J \sim 59$ meV. However this value does not correspond to any of the experimentally determined coupling strengths. The linewidths of these higher energy modes (50 and 96 cm^{-1}) are also smaller compared to the lower energy modes (140 and 190 cm^{-1}). The normalized linewidth of lower energy modes (linewidth of A+B$\sim$ 327 cm^{-1}) is 0.46 (w=E/E_{max}) comparable to the parent compounds of HTSC (w=0.37) [39]. However, this value for higher energy modes (linewidth of C+D $\sim$ 150 cm^{-1}) is w=0.11 which is very small compared to HTSC and higher from the value (w=0.076) for NiF_2, a canted AF [41]. This suggest that the higher energy modes could be due to 2-phonon scattering while the lower energy modes are from magnetic scattering.

3.2.6 Resonance Effect

Similar to Sr_2IrO_4, in $Sr_3Ir_2O_7$ the weakly hybridized states of the transition metal oxide coordinations form narrow bands with a highly structured density of states. Therefore, RRS, in which these energy scales coincide to the photon energy of the incident Laser radiation, can be observed in $Sr_3Ir_2O_7$. In Fig. 3.24 we show the Raman spectra obtained with incident Laser energies of 632 and 532 nm. Due to

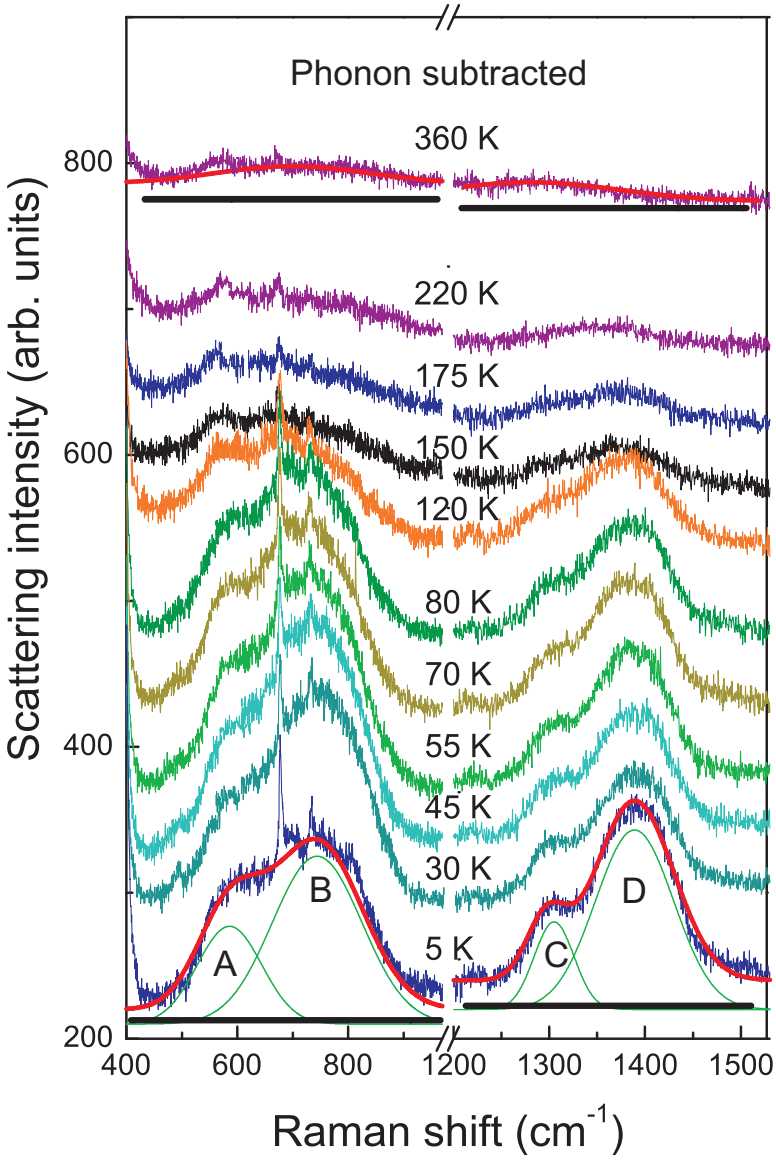

Figure 3.23: Temperature dependence of observed broad modes of $Sr_3Ir_2O_7$ in xu polarization. Phonons are subtracted and spectra are vertically shifted for clarity.

the sample size a detailed resonance study could not be performed. However, a dramatic resonance effect is evident in our data. The phonons at 285, 592, and 677 cm^{-1} are strongly suppressed with red Laser (632 nm). Moreover, DOS like modes at around 1400 cm^{-1} also could not be seen in the measurements done with red Laser. On the other hand, the broad feature centered at 700 cm^{-1} is enormously enhanced in intensity and broadened with red Laser. This might be due to a fluorescence-like charge excitation overlapping a magnetic excitation.

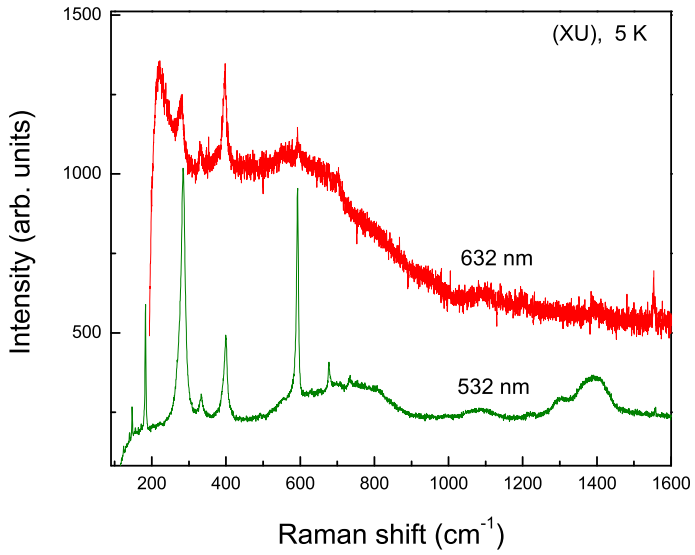

Figure 3.24: Resonance Raman scattering in $Sr_3Ir_2O_7$

3.2.7 Summary

To summarize, we have presented unconventional excitation spectrum in a spin-orbit entangled Mott insulator $Sr_3Ir_2O_7$. The system shows very prominent phonon anomalies, i.e. dramatic shift of phonon at 285 cm^{-1} (9 %), additional modes observed at low temperature (333 and 733 cm^{-1}) and unusual 2-phonon

scattering ($1400\,cm^{-1}$). Moreover, we identified a mode around $700\,cm^{-1}$ as a candidate a for two-magnon scattering ($\sim 700\,cm^{-1}$) in this bilayered iridate which has a collinear AF order with moments along $c-$axis. RRS gives hints about the band structure of this novel $5d$ system.

3.3 The Quasi-1D system $BaIrO_3$

3.3.1 Crystal Structure

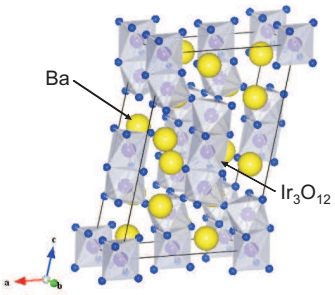

Figure 3.25: Crystal structure of $BaIrO_3$.

There are many studies about the crystal structure of $BaIrO_3$ [57, 58]. Siegrist et al. study the crystal structure of $BaIrO_3$ using a four-circle diffractometer and a small untwinned crystal grown in a molten $BaCl_2$ flux [59]. Single crystal studies revealed that the space group of $BaIrO_3$ is $C2/m$ with unit cell parameters: $a = 10.0052(4)$ Å, $b = 5.7514(2)$ Å, $c = 15.1742(7)$ Å, and $\beta = 103.274(5)°$. The structure of $BaIrO_3$ is derived from the nine-layer $BaRuO_3$-type clusters with a monoclinic distortion. The clusters are combined via vertices to form columns parallel to the c-axis with a symmetric arrangement in the ab plane [60]. In other words, three face-shared IrO_6 octahedra are linked by terminal vertices to the other trimeric clusters along the c-axis. Ba atoms mostly remain in the 12-coordinated sites. The IrO_6 octahedra show small variations in the Ir-O distances from 1.975 Å to 2.043 Å. Due to the presence of two crystallographically distinct clusters, the Ir-Ir distances are slightly different, i.e. 2.616 and 2.633 Å for the intracluster distance, and 3.958 and 3.972 Å for the intercluster distances. As a result of monoclinic distortion, the Ba coordination polyhedra are further

distorted, yielding distances of Ba-O varying from 2.689 Å to 3.499 Å[59].

3.3.2 Electronic and Magnetic Properties

Measurements of electrical resistivity, optical conductivity, and X-ray diffraction of $BaIrO_3$ using single crystal samples carried out by Cao et al. indicate that the ferromagnetic transition of $BaIrO_3$ at 175 K is accompanied by charge density wave formation [5]. Generally speaking, charge density wave is a phenomenon which is observed in low dimensional metals having nesting at Fermi surfaces [61, 62, 63, 64]. Moreover, weak ferromagnetism related to the spin polarization occurs in metals with high density of states $N(E_f)$ at the Fermi level [65, 66, 67, 68]. The magnetic susceptibility of $BaIrO_3$ is reported to be temperature independent above ∼180 K and showing Pauli paramagnetic behavior which indicates that $BaIrO_3$ is supposed to be metallic above ∼180 K [69, 70]. Nevertheless, resistivity measurements show that the resistivity above 175 K is almost constant along the c-axis and increases slightly with decreasing temperature in the ab-plane which is unexpected for metals. A similar effect is observed in the layered $Sr_6V_9S_2O_2$ which is a localized 2D metal. Whangbo et al. suggest that $BaIrO_3$ could be also weakly localized metal [71]. They investigated the band structure of $BaIrO_3$ (see Fig. 3.26) by using Hückel tight-binding model. The t_{2g}-block bands contain 36 bands as there are 12 formula units per unit cell. With an average oxidation state of Ir^{4+} in $BaIrO_3$, there are 60 d-electrons per unit cell to fill the t_{2g}-block bands. $BaIrO_3$ is metallic as the lower-lying group of 32 bands is not filled completely which is not consistent with the experimental result of Cao et al.[71]. To solve this contradiction, Whangbo et al. suggest that $BaIrO_3$ is

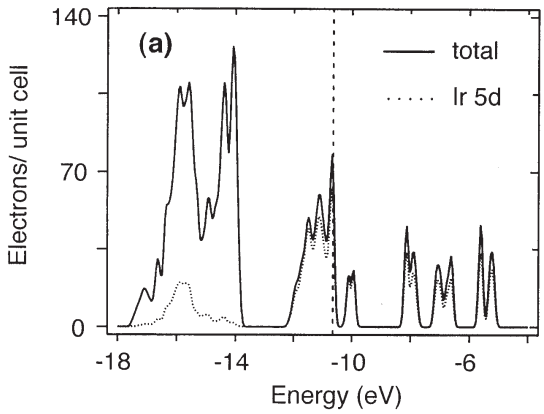

Figure 3.26: Band structure of $BaIrO_3$.

a weakly localized metal above 175 K. Electron localization leads to an electron wave function of finite length L. Hence, the system behaves like an insulator, its charge transport happens through hopping and its resistivity increases strongly with decreasing temperatures in a logarithmic way for a 2D system [71, 72]. Structural distortions in $BaIrO_3$ that are related to the twisting and bending of Ir_3O_{12} trimer units may be the reason for the weak localization. Calculations by Whangbo et al. and Maiti also show that the Fermi surface of $BarIrO_3$ contains strongly warped cylinder-like pieces that are partially nested and hence can give rise to a charge density wave formation [73]. These studies support the observation that the ferromagnetic transition of $BaIrO_3$ at 175 K is accompanied by a charge density formation. Early studies on the magnetic structure of $BaIrO_3$ suggest that the weak ferromagnetism observed in this compound results from canting of antiferromagnetically coupled spins [69, 74]. It is claimed that antiferromagnetism comes from the tilting of Ir_3O_{12} trimers along c-axis. Recently Cao et al. study magnetic properties of $BaIrO_3$ together with the transport, optical and structural properties. Their essential findings about magnetic and transport

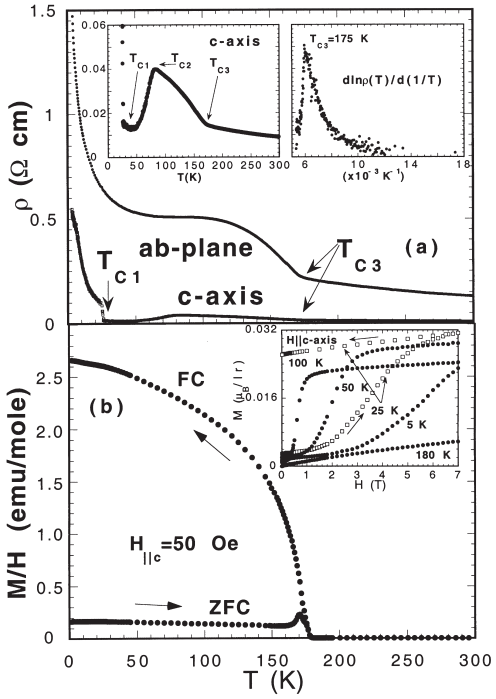

Figure 3.27: Resistivity (a) and magnetization (b) of $BaIrO_3$ measured within and perpendicular to the *ab*-plane [5].

properties of $BaIrO_3$ are summarized in Fig. 3.27. $\rho_{ab}(T)/d(1/T)$ shows a lambda type anomaly at the ferromagnetic ordering temperature, T_{c3} which is strikingly similar to that seen in the charge density wave forming material $TaSe_4$ [64]. The strong increase in resistivity at the transition temperature points out a localization of charge carriers. The transition at T_{c1} is discussed to be a metal-nonmetal transition. $BaIrO_3$ shows metallic-like behavior for temperatures above 27 K and non-metallic behavior for temperatures below 27 K [75, 76]. A strong anisotropy is also evident in their data. Cao et al. attribute the transition from insulating to metallic conductivity at T_{c2} to a crossover from partial gapping of Fermi surface at T_{c3} toward eventual full gapping at T_{c1}. This transition temperature is unchanged and resistivity anomaly is not broadened in magnetic fields up to 10 T, unlike most ferromagnetic transitions which are accompanied by a short range magnetic order. Anomalies in the temperature dependence of X-ray diffraction spectrum [5, 77, 78] points out that the ordered magnetism is driven by a charge density wave formation or induced by the partial Fermi surface gapping accompanied by lattice distortions at T_{c3}. However, presence of an orbital ordering below T_{c3} maybe also be possible. In a perfectly symmetric octahedra, the states are split into a lower t_{2g} triplet and an excited e_g doublet. Only the t_{2g} orbitals play a role, because the exchange between $5d$ electrons is too small to align the spins into a $S = 5/2$ (first Hund's rule). The orbital ordering maybe facilitated by lifting the degeneracy of the t_{2g} orbitals via a lattice distortion of the Jahn-Teller type [79].

The influence of doping on magnetic and electronic structure of $BaIrO_3$ has also been studied [79]. It is found that dilute Sr doping dramatically suppresses the Curie temperature T_C, and instantaneously leads to a nonmetal-metal transi-

tion at high temperatures. It is possible to tune magnetic and transport properties by slight alternations in lattice parameters. Moreover, there are several reports about the effect of pressure on electronic, magnetic, and structural properties of $BaIrO_3$ [80, 81, 82]. Zhao et al. observe that the electrical resistivity increases for increasing pressure and Curie temperature T_C is suppressed by high pressure. The small relative pressure dependence $\partial ln T_c/\partial P$ is attributed to the weak itinerant ferromagnetism of $BaIrO_3$ [80]. Korneta et al. observe that a robust metallic state is induced by merely 4% Gd doping of $BaIrO_3$ while a pressure of 10-12 kbar reinstates the insulating ground state. The effect of doping can be understood with an impurity band formation in a semiconductor but pressure dependence contradicts with this picture. Probably changes in bond lengths and angles are responsible for the metal-insulator transition [82].

3.3.3 Experimental Details

$BaIrO_3$ single crystals with approximate dimension of $1 \times 0.5 \times 0.5\,mm^3$ are grown by using a flux method by the group of Hide Takagi at RIKEN Tokyo. Crystals are cleaved to establish a virgin, optically flat surface. A later cleaning of these surfaces using acetone or methanol is not advisable due to its deteriorating effect on the sample. Raman spectroscopic studies are performed in quasi-backscattering geometry in *ac*-plane with a solid-state laser ($\lambda = 532\,nm$ and 4 mW laser power) as excitation light source.

Measurements are carried out in an evacuated, closed-cycle cryostat. The spectra are collected via a triple spectrometer (Dilor-XY-500) and a micro Raman setup (Horiba Labram) equipped with a liquid nitrogen cooled charge coupled

device (CCD) detector. The measurements have been performed with a spectral resolution of 3-4 cm^{-1} using a slit width of $d = 100\,\mu\mathrm{m}$.

3.3.4 Properties of the Phonon Spectrum

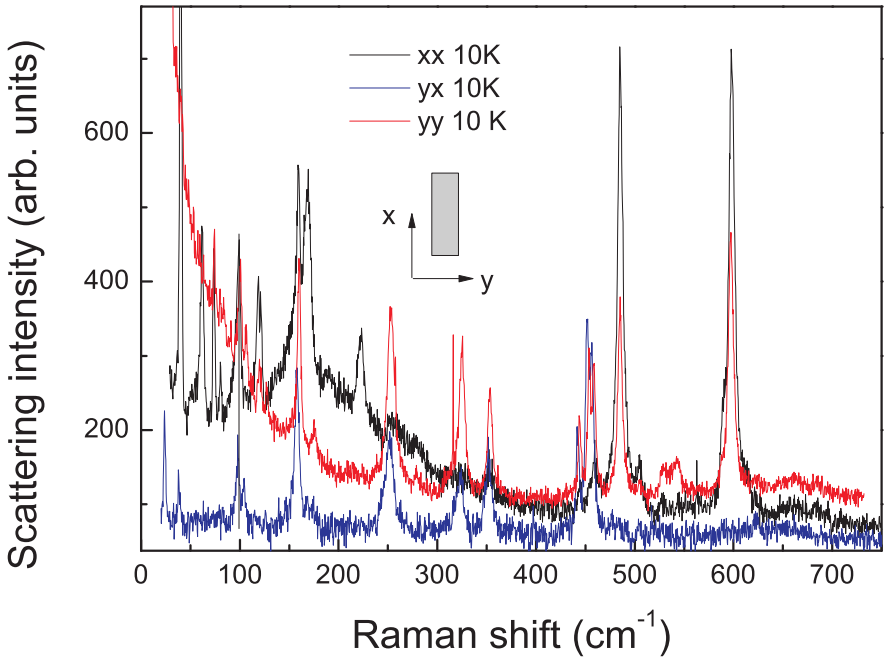

Figure 3.28: Polarization dependence of Raman spectra of $BaIrO_3$.

The factor group analysis predicts forty-two Raman active modes for the space group $C2/m$, see Table. 3.4.

Fig. 3.28 compares Raman spectra for polarization parallel (xx) and perpendicular (yy) to the chain direction at 10 K. Totally 27 modes have been observed in different polarization geometries, for details see Table 3.5. In polarization parallel to the chain (xx), phonons are superimposed by a broad continuum. Moreover in polarization perpendicular to the chain, a strong quasi-elastic scattering is observed. Therefore, the strong polarization dependence of background points out

Table 3.4: Raman active modes according to the factor group analysis for the $C2/m$ structure.

Wyckoff Positions	Raman active modes		Total
Ir1 (4i)	2 A_g	1 B_g	3
Ir2 (2a)	-	-	0
Ir3 (4i)	2 A_g	1 B_g	3
Ir4 (2d)	-	-	0
Ba1 (4i)	2 A_g	1 B_g	3
Ba2 (4i)	2 A_g	1 B_g	3
Ba2 (4i)	2 A_g	1 B_g	3
O1 (4i)	2 A_g	1 B_g	3
O2 (8j)	3 A_g	1 B_g	4
O3 (4i)	2 A_g	1 B_g	3
O4 (8j)	3 A_g	1 B_g	4
O5 (8j)	3 A_g	1 B_g	4
O6 (4i)	2 A_g	1 B_g	3

to anisotropic electronic polarizability due to the quasi-one-dimensional nature of $BaIrO_3$.

The temperature dependence of Raman response Imχ is shown in Fig. 3.29, which is corrected by Bose thermal factor $[1+n(\omega)] = [1 - exp(-\hbar\omega/k_BT]^{-1}$ from the measured Raman scattering intensity. At low temperatures where the system is in insulating state, phonons are rather sharp and strong. However, at high temperatures modes get broader and weaker due to the screening by conduction electrons and due to the thermal fluctuations (anharmonicity). The phonon modes show a number of interesting and anomalous changes in frequency and linewidth as a function of temperature. For a quantitative analysis, modes are fitted by Lorentzian profiles. The resulting frequencies are shown on Fig. 3.30.

For decreasing temperatures, the 42 and 75 cm^{-1} modes undergo a giant energy shift by 9% and 3%, respectively. Such frequency shift is much larger than the several cm^{-1} expected for anharmonic phonon-phonon interactions. Noticeably, the 224 and 590 cm^{-1} modes show even a softening with decreasing tempera-

Table 3.5: Raman active modes observed in $BaIrO_3$.

Frequency (cm^{-1})	Polarization			Comments
	xx	yx	yy	
23	-	+	-	
42	+	+	-	hardening 9 %, Gauss-shape
64	+	-	-	asymmetric, T<140 K
76	+	+	+	hardening 3 %, Gauss-shape
82	+	-	-	T < 80 K
101	+	-	+	asymmetric T <160 K
104	-	+	+	weak, might be B_g
121	+	-	+	asymmetric
123	+	-	+	T < 80 K
127	-	-	+	might be B_g
161	+	+	+	hardening 1.5 %
172	+	-	+	asymmetric
224	+	-	-	
255	+	+	+	Asymmetric, T < 60 K
278	-	-	+	weak, B_g
322	-	+	+	
354	+	+	+	T < 140 K
445	+	+	+	T< 175 K
451	-	+	+	T<80 K
455	-	+	+	T<50 K
460	+	-	-	hardening 1.5 %
487	+	-	+	hardening, intensity
506	+	-	+	hardening 1 %
528	-	-	+	T< 60 K
540	-	-	+	splits T<40 K
590	+	-	+	shoulder T < 140 K
600	+	-	+	

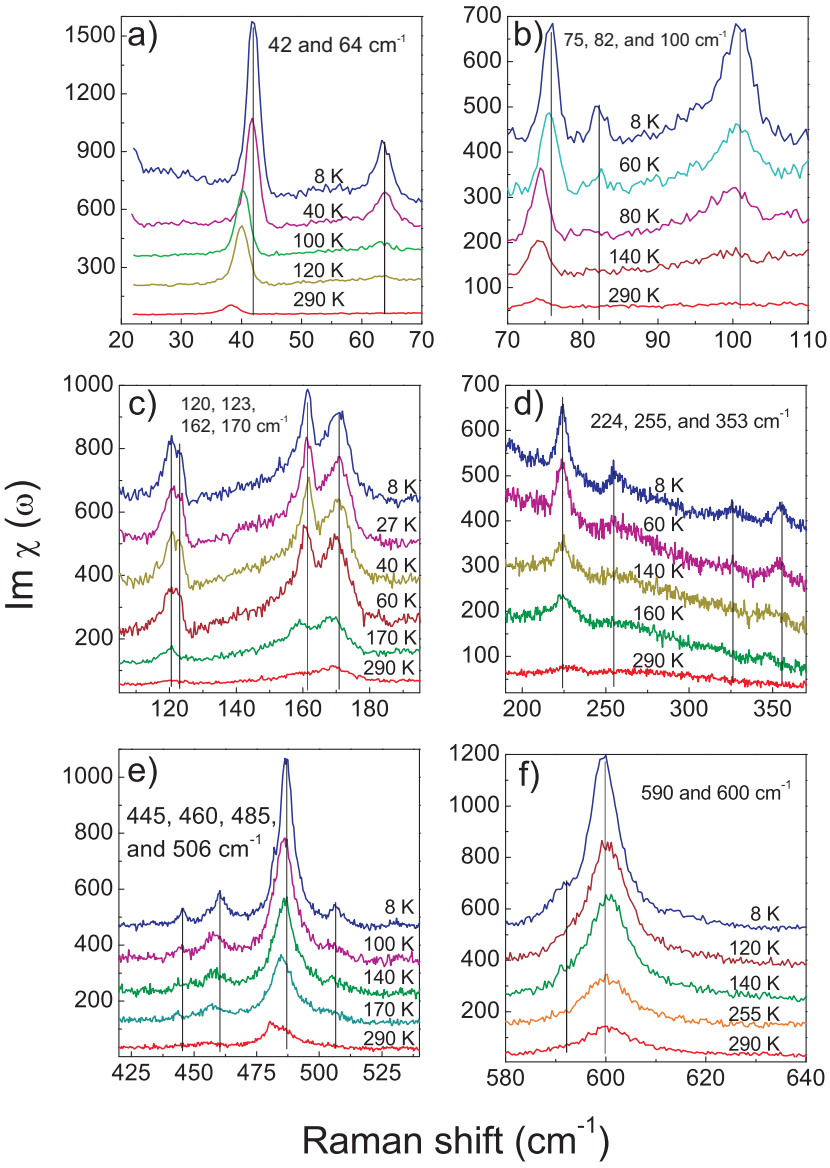

Figure 3.29: Temperature dependent Raman spectra of $BaIrO_3$.

tures, which is opposite to the expected hardening. However, the phonon energies hardly change above charge density wave transition temperature T_{CDW}=185 K. These anomalous frequency shifts might be due to the charge density wave like lattice instability which is observed also in another quasi-1D system $BaVS_3$ [83]. Modes at 64, 82, 100, 255, 353, and 445 cm^{-1} vanish with increasing temperatures all below T_{CDW}=185 K, see Fig. 3.30. Notably, the mode at 123 splits below 80 K. New modes showing up at low temperatures might be due to a zone folding of zone boundary modes to the Γ point. Such a zone-folded mode implies the presence of a new periodicity.

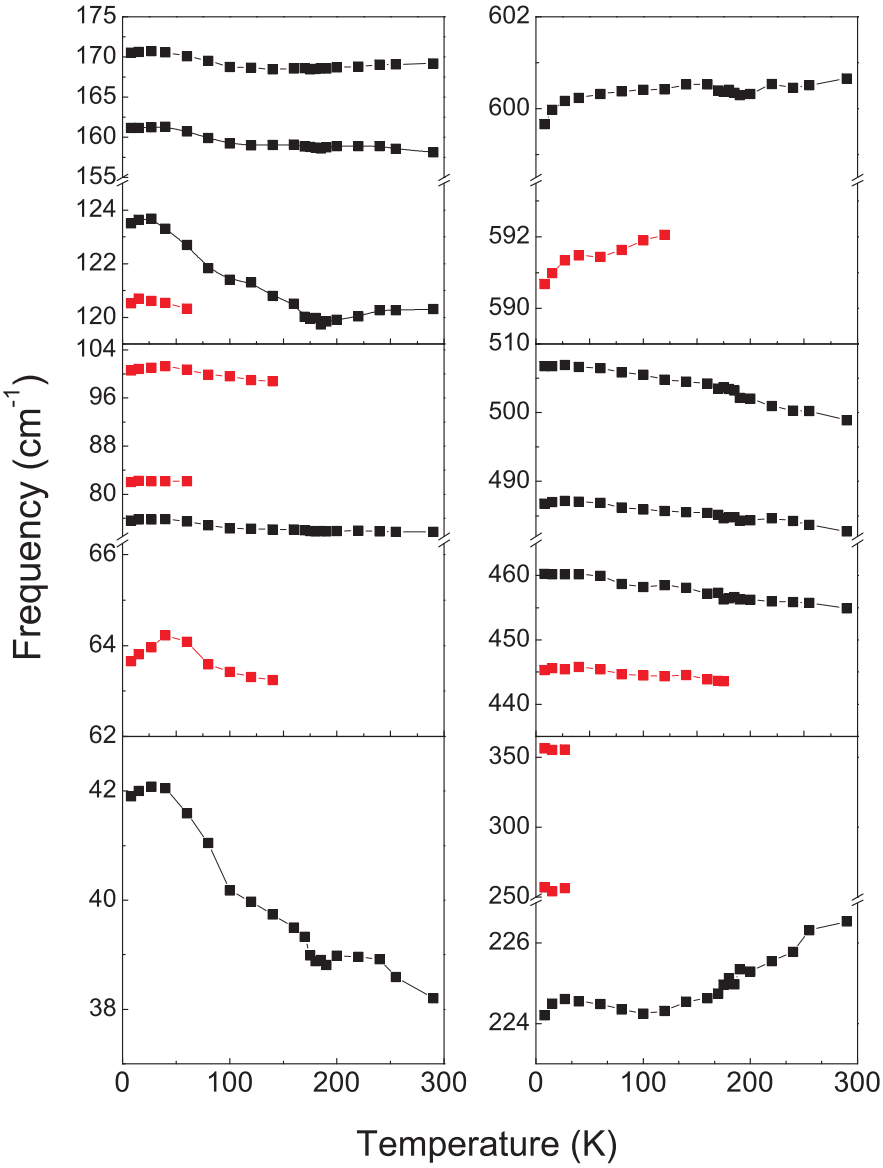

Figure 3.30: Phonon frequencies of $BaIrO_3$ as a function of temperature. Red symbols are used for the modes that show up at only below a certain temperature.

3.3.5 Electronic Raman scattering in $BaIrO_3$

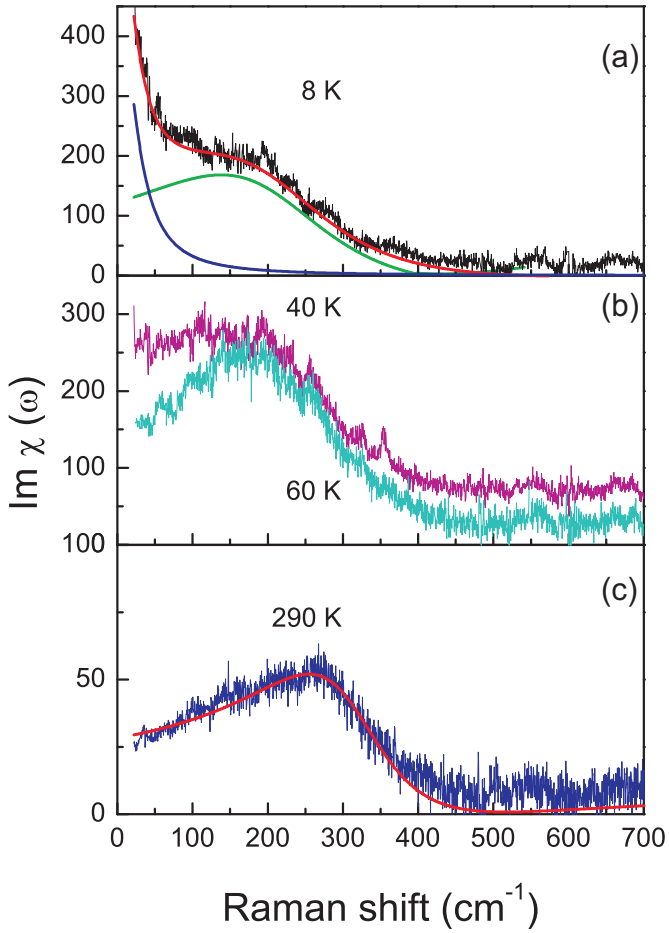

Figure 3.31: Temperature evolution of electronic scattering spectrum.(a) the black curve is the phonon subtracted Raman spectrum, the blue solid curve is the Gaussian fit, the green solid line is the CD model fit, and the red solid line is the sum of Gaussian and CD model. (b) pink and cyan curves are the phonon subtracted Raman spectra measured at 40 and 60 K, respectively. (c) the blue curve is the phonon subtracted Raman spectrum measured at 290 K and the red solid line is CD model fit.

Here we will focus on the temperature evolution of the electronic scattering. $BaVS_3$ is a quasi-one-dimensional metallic system with a metal-insulator transition which is reported to show large changes in the optical phonon spectrum, a central peak, and an electronic Raman scattering continuum that evolves in

a three-step process in a very manner compared to $BaIrO_3$ [83]. Therefore, we believe that the electronic scattering in $BaIrO_3$ is largely analogous to the $BaVS_3$. The electronic Raman response is well fitted by a collision-dominated (CD) model, $\mathrm{Im}\chi \propto B\omega\Gamma/(\omega^2+\Gamma^2)$ at high temperatures as the system is in metallic phase [83] same as it is in $BaVS_3$. Here B is the scattering amplitude and Γ is the carrier scattering rate. Approaching low temperatures, a broad elastic-scattering maximum dominates, which fits to a Gaussian profile. Similar to $K_{0.3}MoO_3$, a typical charge density wave forming system [84], this might be a central peak originating from the second-order structural phase transition [85]. We find that only at low temperatures, the background scattering is well fitted by the sum of the CD (electronic response) and the Gaussian profile (central peak-blue solid curve on Fig. 3.31.(a)). The fits are depicted in Fig. 3.31. The intensity of the central peak decreases rapidly and disappears at temperatures above 40 K. This feature indicates the presence of electronic and structural fluctuations. Surprisingly, no well-defined soft mode shows up below T_{CDW}. The high-temperature metallic state differs from simple metals due to the CD scattering with a carrier scattering rate $\Gamma = 250\,\mathrm{cm}^{-1}$. The low energy electronic Raman response can not be only due to metallic A_{1g} electrons because of the screening effect by itinerant electrons [86]. Thus, the electronic scattering comes from spin(orbital) fluctuations of the localized E_g electrons. This suggests that the electronic correlations are the reason of the metal-insulator transition.

At temperatures above 40 K, the quasi-elastic tail (central peak) is totally suppressed and electronic scattering can be fitted only by CD model, where the CD mode reaches its highest intensity. A continuous reduction in the electronic density of states at the Fermi level E_F might be the reason for diminishing the

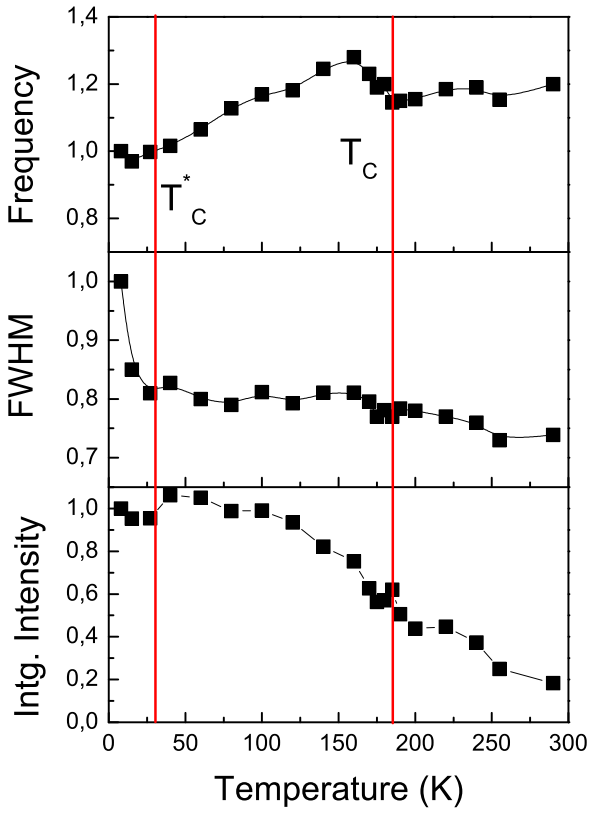

Figure 3.32: Normalized integrated intensity, FWHM and frequency of CD response as a function of temperature.

central peak. The central peak is associated with the decay of a soft mode into acoustic phonons or phonon density fluctuations as the linewidth of the phonons also increase for increasing temperatures. The large linewidth of the CD mode indicates persisting structural fluctuations. Temperature dependence of the CD response due to localized E_g electrons at Fermi surface is gradual, see Fig. 3.32.

In the insulating phase, where the system is fully gapped [5], there is almost no shift in phonon energies. However, the linewidth of the CD response decreases steeply. This is consistent with the lack of a long range magnetic order. The

energy of the CD mode reaches a maximum at around T=185 K which is the magnetic transition temperature. Above this temperature, as the system is in metallic phase, the intensity, frequency and linewidth of the CD response drop gradually as it is expected. This is due to the closing of the insulating gap and the reduction of density of states at the Fermi surface.

3.3.6 Summary

We have demonstrated temperature dependent Raman data of $BaIrO_3$ in which strong phonon anomalies are evident. Our Raman data proves that these anomalies are induced by structural distortions and electronic fluctuations in the system. $BaIrO_3$ goes through a temperature driven metal-insulator transition accompanied by a charge density wave formation which is highly anisotropic. We have succeeded to observe the charge density wave formation in this system by means of broad low energy signal in electronic Raman scattering. A broad maximum with a lineshape fitted by CD model due to the scattering by formation of charge density wave has been observed.

Chapter 4

Summary

In this thesis, we have first presented RRS data of the SOC dominated Mott insulator Sr_2IrO_4. Our data show a sharp resonance of the phonon intensity at 2.5 eV and other anomalies which are due to an O2p-Ir t_{2g} charge transfer excitation across the Mott-Hubbard gap. We attribute the observed temperature dependence to a spectral weight shift caused by the lowest electronic levels in the optical gap. Magnon scattering crosses over to a broad incoherent scattering contribution with an Laser excitation energy above the resonant threshold energy of 2.5 eV. This crossover is attributed to the proximity of the spin excitations to charge modes at the top of the Mott-Hubbard gap. This intermixing is a direct consequence of the dominating spin orbit coupling. The maximum in the incoherent exciton regime is extremely broad. This could be due to metastable electronic configurations such as spin/charge polarons that are induced by the optical absorption process. The formation of polarons may induce resonant Raman scattering as well as other processes such as long-living topological excitations or solitons [43].

Secondly, we discussed unconventional excitation spectra of $Sr_3Ir_2O_7$. Phonon anomalies were evident in Raman data, i.e dramatic frequency shift of the mode at 285 cm^{-1} (9%), additional modes observed only at low temperature (333 and 733 cm^{-1}), and unusual 2-phonon scattering (1400 cm^{-1}). Furthermore, we have observed a broad maximum centered at 700 cm^{-1} which we attribute to two-magnon transition along the *c*-axis as this bilayer iridate has a collinear AF order with moments along *c*-axis. Eventhough the crystal structures of $Sr_3Ir_2O_7$ and Sr_2IrO_4 are very similar, the band structures and band gaps are significantly different for these two compounds. Therefore, no sign for the intermixing of charge modes to the spin excitations has been observed in $Sr_3Ir_2O_7$. A detailed RRS study is possible only with high quality single crystal samples. The powder samples of $Sr_3Ir_2O_7$ have restricted us to perform only a brief RRS. Raman spectrum obtained with red and green Lasers are significantly different pointing out to a complex and hybridized band structure.

Thirdly, we demonstrated temperature dependent Raman data of the quasi-1D system $BaIrO_3$. At low temperatures many additional modes were observed. These modes together with strong frequency shifts point out a temperature dependent structural distortions and electronic/magnetic fluctuations in the system. $BaIrO_3$ goes through a temperature driven metal-insulator transition accompanied by a charge density wave formation which is highly anisotropic. Electronic Raman scattering revealed the formation of a charge density wave in this system. The broad maximum with a lineshape fitted by the collision dominated model due to the scattering by a formation of charge density has been observed with light polarization parallel to the chain direction.

The presented PhD thesis demonstrates interesting cases of correlated electron

systems in which spin, lattice, and charge degrees of freedom are closely entangled.

Chapter 5

Appendix

5.1 The Hyperkagome System $Na_4Ir_3O_8$

5.1.1 Crystal Structure

Okamoto et al. succeeded to refine the powder XRD pattern with the cubic $Na_4Sn_3O_8$ structure as shown in Fig. 5.1(b). The crystal structure of $Na_4Ir_3O_8$ is shown in Fig. 5.1(a) which is derived from spinel oxides, AB_2O_4. The B-sublattice of spinel oxides forms a so-called pyrochlore lattice, a network of corner shared tetrahedra [6]. Each tetrahedron in the B-sublattice is occupied by three Ir and one Na (Na1) in $Na_4Ir_3O_8$. These Ir and Na ions are ordered in a fascinating pattern resulting in a 3D network of corner shared Ir triangles, called hyperkagome as depicted in Fig. 5.1(c). Equivalent Ir sites and Ir-Ir bonds give rise to a substantial geometrical frustration. It should be noted that chirality in hyperkagome lattices leads to two structures $P4_132$ (Fig. 5.1(c)) and $P4_332$ (Fig. 5.1(d)).

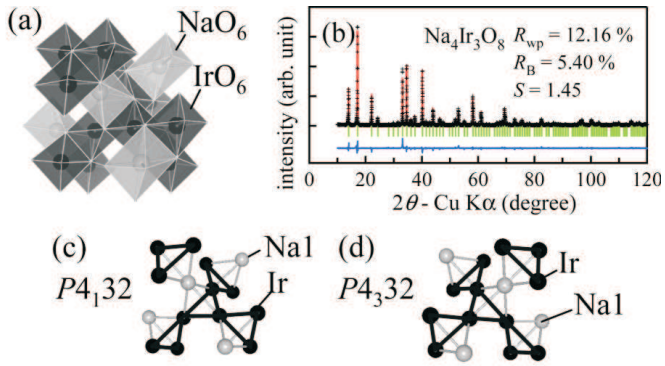

Figure 5.1: (a) Crystal structure of $Na_4Ir_3O_8$, (b) The XRD pattern of $Na_4Ir_3O_8$ at room temperature, two different space groups $P4_132$(c) and $P4_332$(d) [6].

5.1.2 Electronic and Magnetic Properties

Norman et al. calculate the electronic structure of $Na_4Ir_3O_8$ using LDA method and they apply a tight binding fit in order to estimate the exchange integrals. Their calculations reveal that O1 states form a narrow complex of bands ranging from -8.2 to -6.7 eV, followed by the wider O2 branch ranging from -6.7 to -3 eV. A gap of 1.9 eV to the t_{2g} branch of iridium d bands ranging from -1.1 to 0.4 eV is evident in their data. Crystal field also creates a gap of 1.9 eV to an e_g branch ranging from 2.3 to 3.6 eV. The higher energy states are mainly from sodium sites. They also find that Fermi surface is composed of two (electronlike) pockets about the R point, two about the M point (holelike), and one around the Γ point (holelike) [87]. Moreover, SOC strongly influences their results. After including SOC the t_{2g} states split into a lower branch of 48 bands and an upper branch of 24 bands which means number of bands is doubled due to the breaking of the inversion symmetry. The upper t_{2g} band is found to be half filled, with the Ir d states mostly of $j = 5/2$ character with weak admixture of $j = 3/2$. This is similar to the electronic structure of Sr_2IrO_4 and explained in detail also by Chen

et al.[88]. After applying a tight binding model as a fit to the LDA calculations, Norman et al. find the difference of the $t_{2g}-e_g$ energies to be 2.6 eV. The difference from the centroid splitting of 3.43 eV which is reported before is argued to be due to the contributions of the hopping to the splitting [87].

The exchange Hamiltonian of $Na_4Ir_3O_8$ can be written as

$$H_{ex} = (J_d + J_s)S_n \cdot S_m + D^{nm} \cdot (S_n \times S_m) + S_n \cdot \Gamma^{nm} \cdot S_m \tag{5.1}$$

where J_d is the direct exchange between iridium ions, J_s the isotropic component of the superexchange mediated by the oxygen ions, D the Dzyaloshinskii-Moriya interaction, and Γ the anisotropic part of the superexchange [87, 88]. It is found that the direct Ir-Ir exchange, even for the distorted lattice, is surprisingly isotropic and can be defined by $J_d = 2t^2/U$, where $t = \frac{1}{4}t_{dd}^{\sigma} + \frac{1}{3}t_{dd}^{\pi} + \frac{5}{12}t_{dd}^{\delta}$. Norman et al. estimate J_d to be 20 meV which is in a good agreement with the experimental value (28 meV) by Okamoto et al.

The superexchange is responsible for all values in the exchange Hamiltonian except for J_d has large and anisotropic values as reported in Ref. [87]. This would be unlikely if the local site symmetry of Ir ions is purely cubic. There are several reasons for those large values, i.e. the distortion of the octahedra and the mediation of the superexchange between two given Ir ions by an O1 and O2 ion (each ion is in a different environment). The ground state of $Na_4Ir_3O_8$ has been discussed to be spin liquid in many reports [6, 87, 89, 90, 91, 92, 93] however, the first experimental realization of the quantum spin liquid state in geometrically frustrated magnet is achieved by Okamoto et al. They report the temperature dependent magnetic susceptibility $\chi(T)$ which is shown in Fig. 5.2(a). The temperature de-

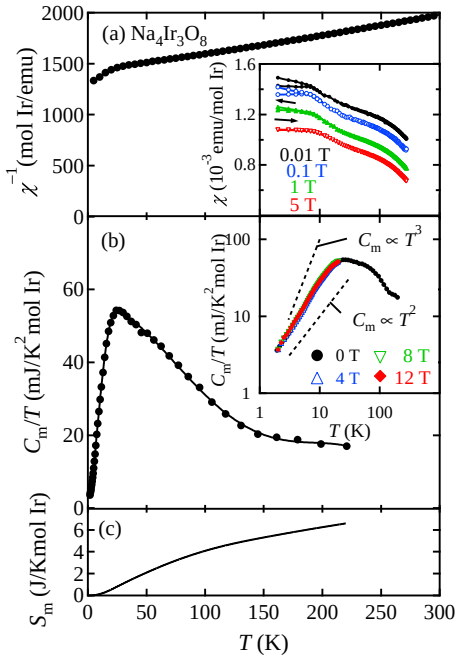

Figure 5.2: Temperature dependence of inverse magnetic susceptibility (a), magnetic specific heat divided by temperature (b) and magnetic entropy (c) [6].

pendence of inverse magnetic susceptibility shows that $Na_4Ir_3O_8$ is a frustrated $S = 1/2$ system with a strong antiferrromagnetic interaction. The Curie-Weiss fit around room temperature resulted in a large Curie-Weiss constant $\theta_W \sim 650\,\mathrm{K}$ and an effective moment of $p_{eff} = 1,96\mu_B$. This value is slightly large for the $S = 1/2$ spins. It is known that in frustrated antiferromagnets, Curie-Weiss behavior persists even below θ_W. Therefore, the observed Curie-Weiss behavior of of $\chi(T)$ below θ_W is consistent with presence of $S = 1/2$ antiferromagnetic spins on a frustrated hyperkagome lattice [6]. It was also shown that despite strong SOC on Ir, the effective spin model is likely of Heisenberg type with SOC induced Dzyaloshinskii-Moriya corrections [91, 92].

5.1.3 Experimental Details

Polycrystalline $Na_4Ir_3O_8$ powder is obtained by using a flux method by the group of Chengtian Lin at MPI-FKF Stuttgart. The powder is sintered to form polycrystalline pellets which are cleaved to establish a virgin, optically flat surface. Raman spectroscopic studies are performed in quasi-backscattering geometry with a solid-state laser ($\lambda = 532\,\text{nm}$ and $1.8\,\text{mW}$ laser power) as excitation light source. The incident and backscattered light are not polarized as the sample was polycrystalline and supposed to show no anisotropy with respect to different polarization of light.

Measurements are carried out in an evacuated, liquid He cooled cryostat. The spectra are collected via micro Raman setup (Horiba Labram) equipped with a liquid nitrogen cooled charge coupled device detector. The measurements have been performed with spectral resolution of 3-4 cm^{-1} using a slit width of $d = 100\,\mu\text{m}$. A detailed Resonance Raman investigation could not be performed as micro Raman setup is equipped only with a solid state Nd:YAG laser (λ =532 nm) and He-Ne (λ =632.8 nm) laser.

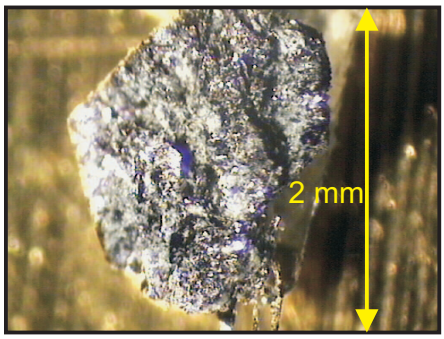

Figure 5.3: Microscope picture of polycrystalline pellet of $Na_4Ir_3O_8$.

5.1.4 Properties of the Phonon Spectrum

Forty-four Raman active modes for $Na_4Ir_3O_8$ with space group $P4_132$ are expected according to a factor group analyses, see Table. 5.1.

Table 5.1: Raman active modes according to the factor group analysis for the $P4_132$ structure.

Wyckoff Positions	Raman active modes			Total
Ir (12d)	1 A_1	3 E	4 T_2	8
Na1 (4b)	-	1 E	1 T_2	2
Na2 (4a)	-	1 E	1 T_2	2
Na3 (12d)	1 A_1	3 E	4 T_2	8
O1 (8c)	1 A_1	2 E	3 T_2	6
O2 (24e)	3 A_1	6 E	9 T_2	18

Raman spectra of $Na_4Ir_3O_8$ measured at different temperatures with unpolarized incident and scattered light (uu) are depicted in Fig. 5.4. As the sample is polycrystalline powder, a detailed polarization dependent Raman study could not be performed. However, the Raman spectra presented in this work are the first results obtained from a hyperkagome system and could give hints about the electronic and magnetic structure of the first realization of a hyperkagome lattice. At lowest temperature (15 K) six weak modes at 162, 198, 218, 245, 265, and 290 cm^{-1} as well as three relatively stronger modes at 464, 576, and 632 cm^{-1} are observed. All observed phonons have sharp Lorentzian-like lineshapes indicating a reasonable sample quality. However, due to the small scattering cross section, only nine out of forty-four modes are detected. Unlike the other iridates which are presented in this thesis (Sr_2IrO_4 and $Sr_3Ir_2O_7$), no broad DOS-like excitations have been observed at high energies, indicating no sign of multi-phonon or magnon processes. However, at low temperature, a broad and weak continuum ranging from 400 up to 630 cm^{-1} which overlaps with mid-energy phonons

is observed. The scattering intensity of this broad feature is temperature dependent, i.e. strongest at 15 K, decrease with increasing temperature and strongly suppressed at room temperature.

The ground state of $Na_4Ir_3O_8$ has been reported to be a gapless spin liquid as discussed before, (see 5.1.2). A true spin liquid with no broken symmetry should show a polarization-independent magnetic Raman response [40]. However, polycrystalline powder samples do not allow to perform such a polarization dependent Raman study.

5.1.5 Summary

We have presented the first Raman scattering data for $Na_4Ir_3O_8$. Nine out of forty-four expected Raman modes are observed. Additionally a broad feature at around 500 cm^{-1} overlapping with the phonons is detected. The energy of this broad signal, 500 cm^{-1} ($\sim$ 62 meV), corresponds to a J value of 20 meV. This is in a good agreement with the experimental and the theoretical values [6, 87]. Temperature dependence of this broad maximum suggests that it is due to short range magnetic fluctuations as the system is reported to be spin liquid in the ground state.

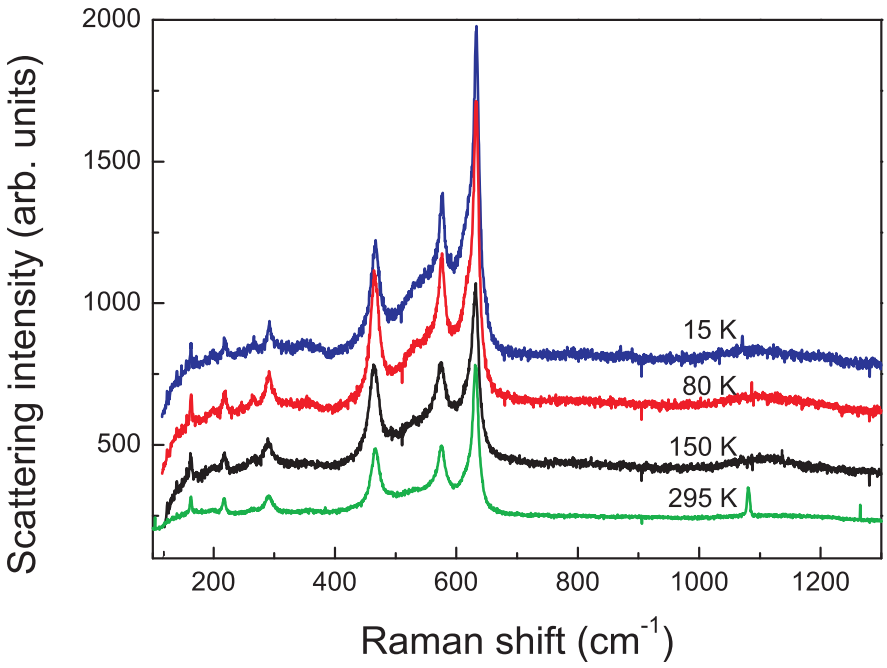

Figure 5.4: Phonon spectrum of $Na_4Ir_3O_8$

Lebenslauf

Persönliche Daten:

Name:	Mehmet Fatih Çetin
Geburtsdatum:	15 November 1984
Geburtsort:	Eleskirt, Türkei
Nationalität:	Türkisch
Telefon:	0049-17685449992
E-Mail:	f.cetin@tu-bs.de

Ausbildung:

01. 2010 - present	Work in the Group of Prof. Lemmens, Institut für Physik der Kondensierten Materie, TU Braunschweig, Deutschland
10. 2006 - 10. 2009	M. Sc. in Applied Polymer Science, Martin Luther Universität Halle-Wittenberg, Deutschland
09. 2002 - 07 2006	B. Eng. in Chemieingenieurwesen, Technische Universität Istanbul, Türkei
09. 1999 - 07. 2002	Gymnasium, Kocaeli Fen Lisesi, Türkei

5. APPENDIX

Mitgliedschaften:

01. 2010 - present	Mitglied der International Graduate School of Metrology, Braunschweig, Deutschland.
02. 2010 - present	Mitglied der NTH School for Contacts in Nanosystems, Deutschland.

Publikationen

- Cetin, M. F., Lemmens, P., Gnezdilov, V., Wulferding, D., Menzel, D., Takayama, T., Ohashi, K., and Takagi, H., Crossover from coherent to incoherent scattering in spin-orbit dominated Sr_2IrO_4, Phys. Rev. B, **85**, 195148(2012)
- Makhal, A., Sarkar, S., Pal, S. K., Yan, H., Wulferding, D., Cetin, M. F., Lemmens, P., Ultrafast excited state deactivation of doped porous anodic alumina membranes, Nanotechnology, **23**, 305705(2012)

References

[1] R. Gutierrez, E. D´, R. Naaman and G. Cuniberti, Phys. Rev. B **85**, 081404 (2012) 1

[2] P. Fazekas, Electron Correlation and Magnetism, World Scientific Publishing, Singapore (1999) 1

[3] J. Kim, D. Casa, M. H. Upton, T. Gog, Y.-J. Kim, J. F. Mitchell, M. van Veenendaal, M. Daghofer, J. van den Brink, G. Khaliullin and B. J. Kim, Phys. Rev. Lett. **108**, 177003 (2012) 2, 25, 30, 38, 43

[4] J. Kim, A. H. Said, D. Casa, M. H. Upton, T. Gog, M. Daghofer, G. Jackeli, J. van den Brink, G. Khaliullin and B. J. Kim, arXiv:1205.5337v1 (2012) 2, 57

[5] G. Cao, J. E. Crow, R. Guertin, P. Henning, C.C.Homes, M. Strongin, D. Basov and E. Lochner, Solid **113**, 657 (2000) 2, 63, 65, 66, 76

[6] Y. Okamoto, M. Nohara, H. Aruga-Katori and H. Takagi, Phys. Rev. Lett. **99**, 137207 (2007) 2, 23, 83, 84, 85, 86, 89

[7] M. Cardona and R. Merlin (Hg.), Light scattering in solids IX, Springer (1983) 2

[8] M. F. Cetin, P. Lemmens, V. Gnezdilov, D. Wulferding, D. Menzel, T. Takayama, K. Ohashi and H. Takagi, Phys. Rev. B **85**, 195148 (2012) 3, 23, 33, 34, 36, 37, 39, 41, 42, 43

[9] C. Timm, Theory of Magnetism, http://www.physik.tu-dresden.de (2011), last accessed: 24/01/13 5

[10] L. H. Thomas, Nature (London, United Kingdom) **117**, 514 (1926) 5, 7

[11] E. U. Condon and G. H. Shortley, The Theory of Atomic Spectra, page 120, 159, Cambridge University Press (1935) 5

[12] D. J. Griffiths, Introduction to Quantum Mechanics, Prentice Hall (2004) 5

[13] C. Moller, The Theory of Relativity, Oxford at the Claredon Press, London (1952) 7

[14] P. Lemmens, G. Güntherodt and C. Gros, Physics Reports **375** (2003) 8

[15] P. Lemmens and K. Y. Choi, Scattering: Inelastic Scattering Technique - Raman, Elsevier Publishers (2005) 8, 10, 18, 20

[16] Bilbao crystallographic server, http://www.cryst.ehu.es/ 15

[17] L. J. P. Ament, G. Khaliullin and J. van den Brink, Phys. Rev. B **84**, 020403 (2011) 23, 25

[18] J. c. v. Chaloupka, G. Jackeli and G. Khaliullin, Phys. Rev. Lett. **105**, 027204 (2010) 23, 24

[19] F. Wang and T. Senthil, Phys. Rev. Lett. **106**, 136402 (2011) 23, 24

[20] M. K. Crawford, M. A. Subramanian, R. L. Harlow, J. A. Fernandez-Baca, Z. R. Wang and D. C. Johnston, Phys. Rev. B **49**, 9198 (1994) 24, 25, 26, 28, 36

[21] B. J. Kim, H. Jin, S. J. Moon, J.-Y. Kim, B.-G. Park, C. S. Leem, J. Yu, T. W. Noh, C. Kim, S.-J. Oh, J.-H. Park, V. Durairaj, G. Cao and E. Rotenberg, Phys. Rev. Lett. **101**, 076402 (2008) 24, 26, 27, 28

[22] S. Chikara, O. Korneta, W. P. Crummett, L. E. DeLong, P. Schlottmann and G. Cao, Phys. Rev. B **80**, 140407 (2009) 24, 29

[23] G. Jackeli and G. Khaliullin, Phys. Rev. Lett. **102**, 017205 (2009) 24, 29

[24] B. J. Kim, H. Ohsumi, T. Komesu, S. Sakai, T. Morita, H. Takagi and A. Tomo, Science **323**, 1329 (2009) 24, 28, 29, 57

[25] K. Ishii, I. Jarrige, M. Yoshida, K. Ikeuchi, J. Mizuki, K. Ohashi, T. Takayama, J. Matsuno and H. Takagi, Phys. Rev. B **83**, 115121 (2011) 24, 28, 41

[26] S. J. Moon, H. Jin, W. S. Choi, J. S. Lee, S. S. A. Seo, J. Yu, G. Cao, T. W. Noh and Y. S. Lee, Phys. Rev. B **80**, 195110 (2009) 25, 28, 33, 42

[27] S. J. Moon, M. W. Kim, K. W. Kim, Y. S. Lee, J.-Y. Kim, J.-H. Park, B. J. Kim, S.-J. Oh, S. Nakatsuji, Y. Maeno, I. Nagai, S. I. Ikeda, G. Cao and T. W. Noh, Phys. Rev. B **74**, 113104 (2006) 25, 28, 33, 42

[28] D. J. Singh, P. Blaha, K. Schwarz and J. O. Sofo, Phys. Rev. B **65**, 155109 (2002) 26

[29] G. Cao, J. Bolivar, S. McCall, J. E. Crow and R. P. Guertin, Phys. Rev. B **57**, R11039 (1998) 28

[30] I. Franke, P. J. Baker, S. J. Blundell, T. Lancaster, W. Hayes, F. L. Pratt and G. Cao, Phys. Rev. B **83**, 094416 (2011) 30, 48

[31] H. Watanabe, T. Shirakawa and S. Yunoki, Phys. Rev. Lett. **105**, 216410 (2010) 30, 39

[32] M. I. Aroya, J. M. Perez-Mato, C. Capillas, E. Kroumova, S. Ivantchev, G. Madariaga, A. Kirov and H. Wondratschek, Zeit f. Kristallogr. **221**, 15 (2006) 32

[33] S. Tajima, T. Ido, S. Ishibashi, T. Itoh, H. Eisaki, Y. Mizuo, T. Arima, H. Takagi and S. Uchida, Phys. Rev. B **43**, 10496 (1991) 35

[34] L. Pintschovius, J. M. Bassat, P. Odier, F. Gervais, G. Chevrier, W. Reichardt and F. Gompf, Phys. Rev. B **40**, 2229 (1989) 35

[35] K.-Y. Choi, P. Lemmens, D. Heydhausen, G. Güntherodt, C. Baumann, R. Klingeler, P. Reutler and B. Büchner, Phys. Rev. B **77**, 064415 (2008) 35, 44, 54

[36] K.-Y. Choi, Y. G. Pashkevich, V. P. Gnezdilov, G. Guentherodt, A. V. Yeremenko, D. A. Nabok, V. I. Kamenev, S. N. Barilo, S. V. Shiryaev, A. G. Soldatov and P. Lemmens, Phys. Rev. B **74**, 064406 (2006) 35, 44, 54

[37] K.-Y. Choi, P. Lemmens, G. Güntherodt, Y. G. Pashkevich, V. P. Gnezdilov, P. Reutler, L. Pinsard-Gaudart, B. Büchner and A. Revcolevschi, Phys. Rev. B **72**, 024301 (2005) 35, 44

[38] P. Lemmens, K. Y. Choi, G. Caimi, L. Degiorgi, N. N. Kovaleva, A. Seidel and F. C. Chou, Phys. Rev. B **70**, 134429 (2004) 35, 44

[39] A. V. Chubukov and D. M. Frenkel, Phys. Rev. B **52**, 9760 (1995) 39, 40, 58

[40] D. Wulferding, P. Lemmens, P. Scheib, J. Röder, P. Mendels, S. Chu, T. Han and Y. S. Lee, Phys. Rev. B **82**, 144412 (2010) 39, 89

[41] E. Meloche, M. G. Cottam and D. J. Lockwood, Phys. Rev. B **76**, 104406 (2007) 40, 58

[42] Y. Fujioka, J. Frantti and M. Kakihana, J. Phys. Chem. B **110**, 777 (2006) 44

[43] S. John and A. Golubentsev, Phys. Rev. Lett. **71**, 3343 (1993) 44, 79

[44] H. Matsuhata, I. Nagai, Y. Yoshida, S. Hara, S. Ikeda and N. Shirakawa, Journal of Solid State Chemistry **177**, 3776 (2004) 46

[45] S. N. Ruddlesden and P. Popper, Acta Crystallographica **11**, 54 (1958) 46

[46] M. Subramanian, M. Crawford and R. Harlow, Materials Research Bulletin **29**, 645 (1994) 46

[47] S. Boseggia, R. Springell, H. C. Walker, A. T. Boothroyd, D. Prabhakaran, S. P. Collins and D. F. McMorrow, Journal of Physics: Condensed Matter **24**, 312202 (2012) 46, 48

[48] S. Y. Jang, H. Kim, S. J. Moon, W. S. Choi, B. C. Jeon, J. Yu and T. W. Noh, Journal of Physics: Condensed Matter **22**, 485602 (2010) 46

[49] S. J. Moon, H. Jin, K. W. Kim, W. S. Choi, Y. S. Lee, J. Yu, G. Cao, A. Sumi, H. Funakubo, C. Bernhard and T. W. Noh, Phys. Rev. Lett. **101**, 226402 (2008) 46, 47, 48, 50

[50] H. J. Xiang and M.-H. Whangbo, Phys. Rev. B **75**, 052407 (2007) 46

[51] G. Cao, Y. Xin, C. S. Alexander, J. E. Crow, P. Schlottmann, M. K. Crawford, R. L. Harlow and W. Marshall, Phys. Rev. B **66**, 214412 (2002) 48, 49, 50, 51, 56

[52] I. Nagai, S.-I. Ikeda, Y. Yoshida, H. Kito and N. Shirakawa, Journal of Low Temperature Physics **131**, 665 (2003) 48

[53] I. Nagai, Y. Yoshida, S. I. Ikeda, H. Matsuhata, H. Kito and M. Kosaka, Journal of Physics: Condensed Matter **19**, 136214 (2007) 48

[54] N. Menyuk, K. Dwight and D. G. Wickham, Phys. Rev. Lett. **4**, 119 (1960) 49

[55] A. V. Mahajan, D. C. Johnston, D. R. Torgeson and F. Borsa, Phys. Rev. B **46**, 10966 (1992) 49

[56] H. C. Nguyen and J. B. Goodenough, Phys. Rev. B **52**, 324 (1995) 49

[57] J. J. Randall and R. Ward, J. Am. Chem. Soc. **81**, 2629 (1959) 62

[58] P. C. Donohue, L. Katz and R. Ward, Inorganic Chemistry **5**, 335 (1966) 62

[59] T. Siegrist and B. L. Chamberland, Journal of the Less-Common Metals **170**, 93 (1991) 62, 63

[60] J. G. Zhao, L. X. Yang, Y. Yu, F. Y. Li, R. C. Yu and C. Q. Jin, Journal of Solid State Chemistry **181**, 1767 (2008) 62

[61] E. Canadell and M.-H. Whangbo, Chem. Rev. **91**, 965 (1991) 63

[62] P. Foury and J. Pouget, Int. J. of Mod. Phys. B **7**, 3973 (1993) 63

[63] J. Dumas and C. Schlenker, Int. J. of Mod. Phys. B **7**, 4045 (1993) 63

[64] G. Grüner, Density waves in solids, Perseus Publishing (1994) 63, 66

[65] E. Stoner, Proc. R. Soc. Lond. A **169**, 339 (1939) 63

[66] J. Janak, Phys **16**, 255 (1977) 63

[67] M. Knecht, H. Ebert and W. Bensch, J. Phys.:Condens. Matter **10**, 9455 (1988) 63

[68] D. Jung, H.-J. Koo and M.-H. Whangbo, J. Mol. Struct. (Theochem) **527**, 113 (2000) 63

[69] R. Lindsay, W. Strange, B. Chamberland and R. O. Moyer, Solid State Communications **86**, 759 (1993) 63, 64

[70] A. Powell and P. D. Battle, J. Alloys Comp. **191**, 313 (1993) 63

[71] M.-H. Whangbo and H.-J. Koo, Solid State Communications **118**, 491 (2001) 63, 64

[72] T. Nakano and I. Terasaki, Phys. Rev. B **73**, 195106 (2006) 64

[73] K. Maiti, Phys. Rev. B **73**, 115119 (2006) 64

[74] W. D. Komer and D. J. Machin, J. Less-Common Metals **61**, 91 (1978) 64

[75] M. A. Laguna-Marco, D. Haskel, N. Souza-Neto, J. C. Lang, V. V. Krishnamurthy, S. Chikara, G. Cao and M. van Veenendaal, Phys. Rev. Lett. **105**, 216407 (2010) 66

[76] M. L. Brooks, S. J. Blundell, T. Lancaster, W. Hayes, F. L. Pratt, P. P. C. Frampton and P. D. Battle, Phys. Rev. B **71**, 220411 (2005) 66

[77] J.-G. Cheng, J.-S. Zhou, J. A. Alonso, J. B. Goodenough, Y. Sui, K. Matsubayashi and Y. Uwatoko, Phys. Rev. B **80**, 104430 (2009) 66

[78] K. Maiti, R. S. Singh, V. R. R. Medicherla, S. Rayaprol and E. V. Sampathkumaran, Phys. Rev. Lett. **95**, 016404 (2005) 66

[79] G. Cao, X. N. Lin, S. Chikara, V. Durairaj and E. Elhami, Physical Review B **69**, 174418 (2004) 66

[80] J. G. Zhao, L. X. Yang, K. Mydeen, F. Y. Li and C. Q. Jin, Solid State Communications **148**, 361 (2008) 67

[81] J.-G. Cheng, J. A. Alonso, E. Suard, J.-S. Zhou and J. B. Goodenough, J. Am. Chem. Soc. **131**, 7461 (2009) 67

[82] O. B. Korneta, S. Chikara, S. Parkin, L. E. DeLong, P. Schlottmann and G. Cao, Phys. Rev. B **81**, 045101 (2010) 67

[83] K.-Y. Choi, D. Wulferding, H. Berger and P. Lemmens, Phys. Rev. B **80**, 245108 (2009) 72, 75

[84] G. Travaglini, I. Morke and P. Wachter, Solid State Communications **45**, 289 (1983) 75

[85] K.-Y. Choi, Y. G. Pashkevich, K. V. Lamonova, H. Kageyama, Y. Ueda and P. Lemmens, Phys. Rev. B **68**, 104418 (2003) 75

[86] A. Zawadowski and M. Cardona, Phys. Rev. B **42**, 10732 (1990) 75

[87] M. R. Norman and T. Micklitz, Phys. Rev. B **81**, 024428 (2010) 84, 85, 89

[88] G. Chen and L. Balents, Phys. Rev. B **78**, 094403 (2008) 85

[89] D. Podolsky, A. Paramekanti, Y. B. Kim and T. Senthil, Phys. Rev. Lett. **102**, 186401 (2009) 85

[90] Y. Zhou, P. A. Lee, T.-K. Ng and F.-C. Zhang, Phys. Rev. Lett. **101**, 197201 (2008) 85

[91] M. J. Lawler, H.-Y. Kee, Y. B. Kim and A. Vishwanath, Phys. Rev. Lett. **100**, 227201 (2008) 85, 86

[92] M. J. Lawler, A. Paramekanti, Y. B. Kim and L. Balents, Phys. Rev. Lett. **101**, 197202 (2008) 85, 86

[93] J. M. Hopkinson, S. V. Isakov, H.-Y. Kee and Y. B. Kim, Phys. Rev. Lett. **99**, 037201 (2007) 85